Pergamon

Geochimica et Cosmochimica Acta, Vol. 68, No. 1, pp. 127–149, 2004

0016-7037/04 $30.00 + .00

doi:10.1016/S0016-7037(03)00416-2

Geochronology, petrology and geochemistry of the granulite xenoliths from Nushan, east China: Implication for a heterogeneous lower crust beneath the Sino-Korean Craton

XIAO-LONG HUANG,*[,1] YI-GANG XU,[1] and DUN-YI LIU[2]

[1]Guangzhou Institute of Geochemistry, Chinese Academy of Sciences, Guangzhou 510640, China
[2]Laboratory of SHRIMP Beijing, Institute of Geology, Chinese Academy of Geological Sciences, Beijing 100037, China

(*Received January* 7, 2003; *accepted in revised form June* 3, 2003)

Abstract—The occurrence of both Archean granulite terrains and granulite xenoliths in Cenozoic basalts from the Sino-Korean Craton (SKC) provides an ideal opportunity to define composition and evolution of continental lower crust of eastern China. The granulite xenoliths in Quaternary basanites from Nushan (southeastern SKC) show a basic-intermediate composition that is distinctly different from mafic granulites from Hannuoba (western SKC). They instead resemble the Archean granulite terrains in terms of mineral and whole rock compositions. Trace element modeling suggests that the "protoliths" of the Nushan granulites were likely subjected to fractional crystallization and assimilation of old crustal components. Zircon SHRIMP U-Pb dating shows at least two episodes in the formation of the lower crust at Nushan. The protoliths of the Nushan granulites were most likely formed at ca. 2.5 Ga and metamorphosed at 1.9 Ga. This late Archean crustal growth was followed by Mesozoic (~140 Ma) basaltic underplating, which was probably coeval with the widespread thermo-tectonic lithospheric reactivation in eastern China. The Nushan granulites are therefore interpreted as dominantly derived from the late Archean crystalline basement and subordinately from the mafic layer that was accreted to the basement during late Mesozoic lithospheric thinning. The consistencies between the depth to seismic Moho and the depth to crust-mantle boundary, and between the calculated V_p (mostly $<$ 7.0 km/s) for granulite xenoliths and the observed velocity structure strongly suggest no obvious high-velocity lowermost crust beneath Nushan and the granulite xenoliths as the dominant components in the lower crust at this locality. The modeled composition of the Nushan lower crust has SiO_2 of ca. 52%, which is more basic than that at Hannuoba ($SiO_2 \approx 58\%$, Liu et al., 2001). Such a compositional difference, in conjunction with contrasting age and seismic velocity structure of the lower crust at the two localities, highlights two fundamentally distinct tectonic domains in the SKC. The data presented in this study also yield implication for the origin of the compositional difference between granulite xenoliths and terrains. *Copyright © 2004 Elsevier Ltd*

1. INTRODUCTION

The nature of the lower crust can be defined through investigating granulite xenoliths entrained in basalts and granulite terrains mainly exposed in Archean-Proterozoic crustal provinces (Rudnick, 1992). These two types of lower crustal samples show significant difference in age, composition, equilibrium pressure and occurrence. For example, granulite xenoliths, which are mostly found in Mesozoic-Cenozoic basalts, are characterized by dominantly mafic compositions and are equilibrated at 10–15 kbar, whereas granulite terrains, which are dominantly of Archean age, have intermediate to silicic compositions and are equilibrated at a shallower level (6–8 Kbar) (Griffin and O'Reilly, 1987; Bohlen and Mezger, 1989; Downes, 1993; Rudnick and Fountain, 1995). Despite decades of efforts, considerable controversy still remains as to the origin of these differences between granulite terrains and granulite xenoliths and in a more general term, the evolution and composition of the continental lower crust.

The Sino-Korean Craton (SKC) in eastern China (Fig. 1) provides a rare opportunity to unravel this long-lasting issue because both Archean granulite terrains and Cenozoic basalts, some of which bear granulite xenoliths, are present in this craton (Jahn et al., 1987; Jahn, 1990; Xu et al., 1998; Chen et al., 2001; Liu et al., 2001; Zhou et al., 2002). Granulitic gneisses or granulites of Archean or early Proterozoic (e.g., Qianxi Formation; Huai'an granulite terrain) are widely distributed in the northern part of the craton (Jahn, 1990; Zhai et al., 1996). A wealth of data has been accumulated on the age and composition of the granulites terrains, some of which are interpreted as exposed lower crustal sections (Zhai et al., 1996). Hannuoba basalts, situated at the northern boundary of the SKC, carry abundant peridotite, pyroxenite and granulite xenoliths. This has stimulated a number of recent studies (e.g., Fan and Liu, 1996; Fan et al., 1998, 2001; Chen et al., 2001; Liu et al., 2001; Zhou et al., 2002) which all have emphasized basaltic underplating at the base of the crust and crust-mantle interaction as mechanisms for crustal growth and evolution. Single zircon U-Pb dating (Fan et al., 1998; Liu et al., 2001) further suggested that this basaltic underplating may be related to the late Mesozoic lithospheric thinning that dramatically affected the lithospheric architecture beneath the SKC (Menzies et al., 1993; Griffin et al., 1998; Xu, 2001).

Another important but less known locality of granulite xenoliths is situated at the southern edge of the SKC (i.e., Nushan; Fig. 1). The granulite xenoliths from Nushan have been selected as target of this study for the following reasons: (1) The peculiar geographic position makes the Nushan granulites as an important source in addition to the Hannuoba xenoliths to

* Author to whom correspondence should be addressed (xlhuang@gig.ac.cn).

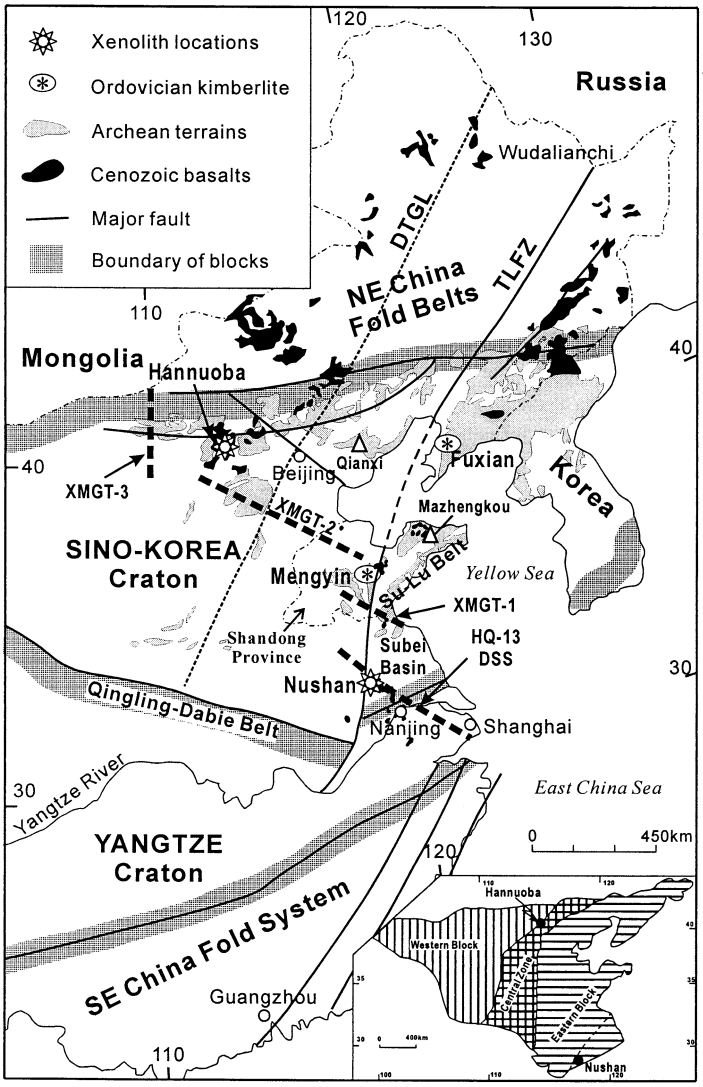

Fig. 1. Sketch map showing simplified tectonic units and location of granulite xenoliths in eastern China (modified after Li, 1994; Xu et al., 1998 and Menzies and Xu, 1998). The distribution of Cenozoic basalts and of Archean terrains in the Sino-Korean Craton is after Liu et al. (1994) and Jahn (1990). The inset illustrates a new tectonic classification of the Sino-Korean Craton (after Zhao et al., 1999). Note that the Archaean Sino-Korean Craton is cut by two major geological and geophysical linear zones: Tan-Lu fault zone (TLFZ) to the east and Daxing'anlin-Taihang gravity lineament (DTGL) to the west. The Deep Seismic Sound profile HQ-13 passes through the Nushan locality, and the Xiangshui to Mandal geo-transect (XMGT) cross entirely the Craton.

define the spatial heterogeneity of the lower crust under the SKC; (2) Preliminary studies show that the Nushan samples differ significantly from the Hannuoba granulites but show some compositional similarities to the Archean granulite terrains (Zhou et al., 1992); understanding compositional diversity in granulite xenoliths is particularly relevant to the xenolith versus terrain issue mentioned above; (3) Seismic refraction/reflection profiling has been conducted at the vicinity of the Nushan locality (Chen, 1988), which allows to constrain the structure of the lower crust by integrating petrologic-petrophysical and geophysical data, a recommended approach in deep geologic studies (Griffin and O'Reilly, 1987; Rudnick and Fountain, 1995); (4) Finally, an affinity assessment of the lower crust beneath Nushan should shed lights on the debate concerning the location of the suture between the North China and South China Blocks in eastern China (Fig. 1; Li, 1994; Chung, 1999; Chung and Li, 2000; Zhang, 2000), because the Nushan granulites represent fragments of the deep crust close to the postulated suture zones.

This paper presents new zircon SHRIMP U-Pb age, petrologic and geochemical data on the Nushan granulite xenoliths. These data, along with geothermobarometric and seismic refraction data, are used to constrain their petrogenesis and to define the chemical composition and structure of the lower crust under the southern SKC. The Nushan granulite xenoliths compositionally resemble the exposed Archean granulite terrains, but significantly differ from the mafic granulite xenoliths from Hannuoba. This not only reveals the spatial heterogeneity

Table 1. The texture, structure and modal mineralogy of analysed granulite xenoliths.

Sample	*D* (cm)	Description	Modes†
NS201	6	banded, fine-grain granoblastic texture with triple junction	Opx_{22} Cpx_{19} Pl_{54} Mt_5
NS202	9	banded, fine-grain granoblastic texture with triple junction	Opx_{12} Cpx_{24} Pl_{52} Mt_{12} (Bi)
NS203	3	banded, fine-grain granoblastic texture with triple junction	Opx_{10} Cpx_{25} Pl_{58} Qz_1 Mt_6
NS204	4.5	banded, heteroblastic texture	Opx_{17} Cpx_{23} Pl_{54} Mt_6 (Apt)
NS205	7	banded, heteroblastic texture	Opx_{12} Cpx_{13} Pl_{65} Qz_5 Mt_5
NS206	5	banded, heteroblastic texture, partially recrystallized	Opx_{12} Cpx_{23} Pl_{55} Mt_{10} (Apt+Bi)
NS207	6	banded, fine-grain granoblastic texture	Opx_{15} Cpx_{12} Pl_{67} Qz_1 Mt_5 (Apt)
NS210	8.5	banded, fine-grain granoblastic texture	Opx_{14} Cpx_8 Pl_{67} Qz_3 Mt_8 (Apt)
NS212	7.5	banded, heteroblastic texture, partially recrystallized	Opx_{12} Cpx_{19} Pl_{59} Qz_3 Mt_7 (Apt)
NS213	7	banded, heteroblastic texture, partially recrystallized	Opx_{13} Cpx_{20} Pl_{59} Qz_1 Mt_7 (Apt)
NS214	17	banded, heteroblastic texture	Opx_{11} Cpx_{12} Pl_{66} Qz_6 Mt_5
NS217	6.5	banded, heteroblastic texture	Opx_{10} Cpx_7 Pl_{65} Qz_{13} Mt_5

† Calculated by point count of more than 2000 points; *D* = Diameter of the Samples; Opx = orthopyroxene, Cpx = clinopyroxene, Pl = plagioclase, Qz = quartz, Mt = Fe-Ti Oxides, Apt = apatite, Bi = Biotite. Minerals in parentheses occur in very small amount.

of the lower crust beneath the SKC and but also provides a clue to understand the compositional contrast between granulite xenoliths and Archean granulite terrains.

2. GEOLOGICAL BACKGROUND

The Sino-Korean Craton is one of the oldest continental nuclei in the world (Jahn et al., 1987; Jahn, 1990; Liu et al., 1992) and the largest cratonic block in China. It covers an area of more than 1500000 km^2, where granulitic rocks of Archean or early Proterozoic are widely distributed (Fig. 1). Two large-scale major geological and geophysical linear zones cut cross the SKC. To the east, the craton is cut by the Tan-Lu Fault Zone (TLFZ) that is associated with important Cenozoic and Mesozoic volcanic activity. To the west, the craton is traversed by the N-S trend Daxing'anling-Taihangshan gravity lineament (DTGL). Two granulite xenolith localities, namely Nushan and Hannuoba, are situated differently with respect to these two major linear zones. Hannuoba lies to the west of the DTGL in the northern boundary of the SKC, whereas Nushan is situated to the east of the DTGL at the southern edge of the craton, proximal to the southern part of the TLFZ (Fig. 1). A deep seismic refraction profile (HQ-13) traverses the Nushan locality (Fig. 1), which shows the present depth to Moho of ca. 30 km at Nushan.

Both Palaeozoic diamondiferous kimberlites and Cenozoic basalts erupted through this craton and provide informations about the Phanerozoic evolution of the lithosphere underneath the SKC. A significant change in thermal gradient of the lithosphere from Palaeozoic ($\sim$ 40 mW/m^2) to Cenozoic ($>$80 mW/m^2) has been estimated by P-T studies of xenoliths and minerals (e.g., garnet and chromite) in Paleozoic kimberlites and in Cenozoic alkali basalts (Griffin et al., 1998; Menzies and Xu, 1998). Present lithospheric thickness in this region is 80–100 km, which is significantly thinner than estimates for the Palaeozoic lithosphere ($>$200 km). This has led to hypothesize replacement of the old, cold, thick, depleted lithospheric mantle by young, hot, thin, and fertile lithospheric mantle accompanied by lithospheric thinning (Menzies et al., 1993; Griffin et al., 1998). Such a thermotectonic event most likely happened during the late Mesozoic (Xu, 2001), consistent with emplacement of voluminous late Mesozoic granites and intermediate to mafic intrusion, followed by extensive Cenozoic volcanism.

The granulite xenoliths studied were collected from a small volcanic cone at Nushan, Anhui Province, which belongs to the Jiashan-Liuhe volcanic complex. The spatial distribution of volcanoes in this region is controlled by the NNE-trending Tan-Lu fault and its adjacent NW-trending basins and faults. Volcanism began in the Palaeocene ($\sim$ 65 Ma) and continued into the Quaternary. The major phase of tholeiitic eruption was associated with formation of the Subei fault-depression basin during the Eocene, whereas alkaline volcanic activity started in the Neogene in the Jiashan-Liuhe region and continued into the Quaternary. The age of the Nushan basalts estimated by K-Ar method is 0.63 Ma (Chen and Peng, 1988) and the lavas are alkali olivine basalt, basanite and nephelinites, showing trace element features similar to those of oceanic island basalts (Liu et al., 1994). Peridotite and pyroxenite xenoliths are abundant in basaltic flow and scoria (Xu et al., 1998; Xu and Bodinier, in press). Subordinate granulite xenoliths are also present (Zhou et al., 1992; Yu et al., 2003) and form the object of this study.

3. SAMPLE DESCRIPTION

The granulite xenoliths are generally fresh and small (usually 2–10 cm in diameter). They show contacts with the host basalts indicating limited interaction with the rocks that carried them up to the surface. All samples are characterized by foliated structure in hand-specimens, which is due to oriented distribution of tabular plagioclase crystals relative to other minerals. The main petrographic and mineralogical characteristics of the analyzed samples are summarized in Table 1. The Nushan granulites are typical of two-pyroxene granulites, and predominantly composed of orthopyroxene, clinopyroxene and plagioclase with subordinate amount of quartz and Fe-Ti oxides (Table 1). But Amphibole or biotite, the most common hydrous phases in Archean granulite terrains of SKC, is almost absent in all Nushan granulites except for very small amount of biotite in NS202 and NS206. All the samples show a mineralogic banding composed of pyroxene-rich and plagioclase-rich layers. Pyroxenes are surrounded by anhedral opaque Fe-Ti oxides, which are distinctively different from Archean granulite ter-

Table 2. Major and trace element data for selected Nushan granulite xenoliths.

	NS201	NS202	NS204	NS205	NS206	NS207	NS210	NS212	NS213	NS214
(wt%)										
SiO_2	50.6	46.4	51.0	54.8	50.7	52.5	52.3	51.4	51.8	55.3
TiO_2	0.72	2.35	1.57	0.82	1.37	1.01	2.29	1.47	1.17	0.97
Al_2O_3	16.2	15.8	17.1	17.8	15.6	17.8	16.4	16.3	16.0	17.4
Fe_2O_3	3.92	8.96	6.28	3.48	6.41	4.87	5.29	6.23	5.04	4.34
FeO	8.07	7.57	5.03	4.30	6.13	5.57	7.60	5.50	6.77	5.60
MgO	6.60	4.90	4.03	4.37	5.10	4.22	2.76	4.22	4.83	3.22
MnO	0.15	0.18	0.14	0.12	0.17	0.22	0.16	0.14	0.19	0.19
CaO	9.24	9.33	8.61	8.13	9.11	8.02	5.83	8.56	8.16	7.29
Na_2O	2.82	2.95	4.08	4.71	3.74	3.72	4.42	4.17	4.00	4.11
K_2O	0.61	0.62	0.80	0.51	0.68	0.79	1.40	0.87	0.68	0.43
P_2O_5	0.19	0.57	0.76	0.35	0.51	0.54	0.72	0.81	0.39	0.39
LOI	0.01	0.08	0.12	0.20	0.04	0.39	0.01	0.03	0.01	0.01
Total	99.2	99.6	99.6	99.6	99.6	99.6	99.2	99.6	99.1	99.2
Mg#	0.54	0.40	0.44	0.55	0.47	0.47	0.32	0.44	0.47	0.42
D.F.		0.67	3.48	3.89	1.82	2.36	3.22	3.23	1.90	2.88
In ppm										
V	111	361	150	97.8	165	139	159	140	165	123
Cr	128	35.2	72.7	73.1	86.9	65.7	28.9	70.1	142	39.6
Co	40.2	46.7	28.9	25.3	29.1	25.4	24.2	31.4	30.6	21.9
Ni	85.6	37.7	56.2	56.7	52.3	35.3	21.6	64.0	52.0	19.1
Ga	17.2	21.4	23.8	21.3	22.9	22.9	22.1	22.6	23.4	21.8
Rb	2.56	5.40	2.87	1.16	2.48	2.26	11.2	3.66	2.06	0.14
Sr	643	813	1552	1803	1397	1334	755	1610	800	975
Y	22.0	22.9	43.6	12.4	52.1	30.7	56.7	49.6	23.9	24.9
Zr	125	328	460	105	443	214	1120	453	247	135
Nb	5.38	6.80	11.8	3.92	10.5	8.58	39.2	11.7	10.6	9.70
Ba	787	1142	1336	909	1296	1206	2123	1423	920	458
Hf	3.02	6.35	11.0	2.40	10.6	4.74	19.6	10.5	5.70	3.53
Ta	0.23	0.28	0.49	0.13	0.40	0.21	1.43	0.41	0.33	0.35
Pb	4.46	4.34	7.44	6.02	5.61	9.86	10.8	6.66	6.54	5.86
Th	0.13	0.59	1.89	0.24	1.27	1.32	1.51	2.10	0.27	0.21
U	0.03	0.11	0.19	0.05	0.13	0.10	0.17	0.17	0.13	0.07
La	21.4	25.6	87.5	29.5	69.9	74.8	80.5	99.7	35.0	32.9
Ce	42.7	53.2	166	59.2	140	150	166	194	71.2	74.9
Pr	5.72	7.50	22.2	8.25	18.3	18.0	20.9	24.3	9.28	10.3
Nd	23.9	33.2	85.1	34.9	75.7	70.9	84.6	97.6	39.1	41.5
Sm	4.83	6.36	14.1	5.91	13.7	11.9	15.6	16.0	7.40	7.84
Eu	1.53	2.86	4.38	2.08	3.95	3.09	3.85	4.30	2.45	2.52
Gd	4.35	5.63	11.4	3.91	11.1	8.29	12.8	12.2	6.17	6.52
Tb	0.69	0.82	1.60	0.53	1.68	1.17	1.90	1.76	0.89	0.91
Dy	3.87	4.29	8.25	2.44	9.17	5.72	10.2	9.11	4.59	4.77
Ho	0.78	0.83	1.67	0.43	1.85	1.04	1.96	1.74	0.87	0.96
Er	2.05	2.07	4.33	1.07	4.86	2.69	5.07	4.46	2.14	2.42
Tm	0.30	0.29	0.63	0.13	0.70	0.36	0.70	0.60	0.29	0.35
Yb	1.94	1.78	4.06	0.87	4.51	2.20	4.47	3.72	1.78	2.30
Lu	0.30	0.27	0.64	0.13	0.71	0.33	0.71	0.58	0.27	0.36
ΣREE	114	145	411	149	356	351	409	470	181	189
$(La/Yb)_N$	7.5	9.7	14.6	22.8	10.5	23.0	12.2	18.1	13.3	9.7
Zr/Hf	41.2	51.7	41.9	43.7	41.9	45.2	57.1	43.2	43.3	38.3
Nb/Ta	23.9	24.2	23.8	30.8	26.4	41.2	27.4	28.3	32.5	27.9
K/Ba	6.4	4.5	5.0	4.7	4.4	5.4	5.5	5.1	6.1	7.8
K/Rb	1980	954	2320	3670	2270	2900	1040	1980	2740	25500
Rb/Sr	0.004	0.0066	0.0018	0.0006	0.0018	0.0017	0.0148	0.0023	0.0026	0.0001

Mg = $Mg/(Mg + 0.85Fe^{tot})$ (Kempton et al., 1997); D.F. = $10.44-0.21SiO_2$-$0.32FeO^{tot}$-$0.98MgO + 0.55CaO + 1.46Na_2O + 0.54K_2O$ (Shaw, 1972); $(La/Yb)_N$ is the chondrite normalized ratio.

rains in the SKC. The mineralogic banding structures were also observed in mafic granulite xenoliths from Hannuoba (Chen et al., 2001) and from the Western Pannonian Basin (Kempton et al., 1997), and may be related to layered or banded structure of original protoliths (Kempton et al., 1997; Chen et al., 2001). Euhedral apatites occur as inclusion in plagioclase in some samples. Most samples show a fine-grained granoblastic texture in which pyroxenes and plagioclases are usually 0.1–0.6 mm in size, and the triple junction of plagioclases or pyroxenes are always observed in these samples. Larger tabular porphyroblast plagioclases (0.7–1.5 mm) in the samples with a heteroblastic texture show deformation twinning, which reflect an incomplete degree of the textural re-equilibration that eventually lead to granoblastic texture.

Table 3. Zircon SHRIMP U-Pb data for NS214.

Spot	Pos	U ppm	Th ppm	Th/U	Pb ppm	f_{206} (%)	$^{207}Pb/^{206}Pb$ $\pm1\sigma$	$^{206}Pb/^{238}U$ $\pm1\sigma$	$^{207}Pb/^{235}U$ $\pm1\sigma$	Apparent ages (Ma) $^{207}Pb/^{206}Pb$	Apparent ages (Ma) $^{206}Pb/^{238}U$
N1-1	c	107	66	0.615	19	0.21	0.1301 ± 14	0.1581 ± 73	2.84 ± 14	2100 ± 19	946 ± 41
N1-2	r	282	186	0.658	58	0.04	0.1295 ± 11	0.1803 ± 73	3.22 ± 14	2092 ± 14	1069 ± 40
N2-1	c	679	782	1.152	340	0.01	0.1548 ± 27	0.3890 ± 138	8.30 ± 34	2399 ± 29	2118 ± 64
N2-2	r	44	35	0.795	19	0.10	0.1162 ± 22	0.3757 ± 157	6.02 ± 29	1899 ± 35	2056 ± 74
N3-1	c	903	717	0.794	354	0.08	0.1376 ± 7	0.3321 ± 110	6.30 ± 21	2197 ± 8	1848 ± 53
N3-2	r	30	16	0.525	15	0.09	0.1376 ± 14	0.4400 ± 190	8.35 ± 38	2198 ± 18	2351 ± 85
N4-1	r	319	177	0.553	47	0.10	0.1154 ± 22	0.1336 ± 48	2.13 ± 9	1886 ± 34	808 ± 27
N5-1	c	642	409	0.637	225	0.02	0.1340 ± 7	0.3075 ± 106	5.68 ± 20	2151 ± 8	1729 ± 53
N6-1	c	200	178	0.889	91	0.06	0.1626 ± 20	0.3689 ± 131	8.27 ± 32	2483 ± 21	2024 ± 62
N6-2	r	13	3	0.192	1	0.67	0.1214 ± 165	0.0747 ± 63	1.25 ± 21	1977 ± 264	464 ± 38
N7-1	m	130	70	0.536	44	0.10	0.1260 ± 14	0.3080 ± 103	5.35 ± 19	2043 ± 19	1731 ± 51
N8-1	c	77	55	0.716	5	0.14	0.1159 ± 59	0.0587 ± 28	0.94 ± 7	1894 ± 94	368 ± 17
N8-2	r	33	20	0.607	1	1.41	0.1113 ± 70	0.0358 ± 18	0.55 ± 5	1821 ± 119	227 ± 11
N9-1	c	160	110	0.686	26	0.08	0.1515 ± 55	0.1391 ± 93	2.90 ± 23	2362 ± 64	840 ± 53
N10-1	c	66	36	0.549	24	0.22	0.1474 ± 23	0.3285 ± 113	6.67 ± 26	2316 ± 27	1831 ± 55
N11-1	m	96	83	0.863	40	0.06	0.1195 ± 50	0.3574 ± 218	5.89 ± 46	1949 ± 77	1970 ± 105
N12-1	c	114	72	0.632	25	0.13	0.1491 ± 40	0.1883 ± 89	3.87 ± 22	2335 ± 47	1112 ± 49
N13-1	m	51	27	0.537	1	0.40	0.1131 ± 65	0.0245 ± 10	0.38 ± 3	1850 ± 108	156 ± 6
N14-1	r	25	14	0.557	2	1.58	0.1180 ± 105	0.0690 ± 36	1.12 ± 12	1927 ± 169	430 ± 22
M1-1	c	174	62	0.354	25	0.03	0.1404 ± 25	0.1343 ± 51	2.60 ± 11	2232 ± 31	813 ± 29
M2-1	r	25	18	0.700	4	1.10	0.1239 ± 66	0.1474 ± 55	2.52 ± 17	2013 ± 98	886 ± 31
M3-1	c	131	108	0.821	65	0.06	0.1445 ± 11	0.4258 ± 167	8.49 ± 35	2282 ± 13	2287 ± 76
M4-1	c	153	153	0.999	70	0.07	0.1505 ± 18	0.3731 ± 125	7.74 ± 28	2351 ± 20	2044 ± 59
M5-1	c	451	306	0.679	163	0.03	0.1432 ± 6	0.3131 ± 144	6.18 ± 29	2266 ± 8	1756 ± 71
M6-1	c	222	89	0.403	52	0.04	0.1393 ± 70	0.2177 ± 80	4.18 ± 27	2219 ± 90	1269 ± 42
M6-2	r	24	16	0.661	3	10.32	0.1286 ± 320	0.1165 ± 75	2.07 ± 55	2079 ± 519	710 ± 44
M7-1	r	328	166	0.506	64	0.58	0.1189 ± 53	0.1757 ± 69	2.88 ± 18	1940 ± 82	1043 ± 38
M8-1	c	101	41	0.409	34	0.03	0.1387 ± 15	0.3127 ± 113	5.98 ± 23	2211 ± 19	1754 ± 56
M9-1	c1	145	101	0.700	59	0.00	0.1412 ± 8	0.3553 ± 177	6.92 ± 35	2242 ± 10	1960 ± 85
M9-2	c2	285	229	0.804	125	0.01	0.1549 ± 7	0.3671 ± 171	7.84 ± 37	2401 ± 81	2016 ± 81

Note: c = core, r = overgrowth rim, m = metamorphic zircon; f_{206}(%) is percent of total ^{206}Pb which is non-radiogenic.

4. ANALYTICAL TECHNIQUES

Analyses of mineral phases were carried out at the Nanjing University with a JEOL Superprobe (JXA 8800M). The operating conditions are as follows: 15kV accelerating voltage, 10 nA beam current and 1 μm beam diameter, a program based on ZAF correction procedure for data reduction.

Whole-rock major element compositions of 10 samples (Table 2) were obtained using X-ray fluorescence (XRF) at the Center Laboratory of Hubei Institute of Geology. These samples were also analyzed

Table 4. Zircon SHRIMP U-Pb data for NS202.

Spot	Pos	U ppm	Th ppm	Th/U	Pb ppm	$f206$ (%)	$^{207}Pb/^{206}Pb$ $\pm1\sigma$	$^{206}Pb/^{238}U$ $\pm1\sigma$	$^{207}Pb/^{235}U$ $\pm1\sigma$	Apparent ages (Ma) $^{207}Pb/^{235}U$	Apparent ages (Ma) $^{206}Pb/^{238}U$
H2-1	eu	261	184	0.705	6	0.45	0.0501 ± 23	0.0225 ± 8	0.1553 ± 93	143 ± 5	143 ± 5
H3-1	eu	191	150	0.784	5	0.83	0.0526 ± 52	0.0214 ± 8	0.1551 ± 171	146 ± 15	137 ± 5
H4-1	eu	201	160	0.796	5	0.24	0.0547 ± 24	0.0214 ± 11	0.1614 ± 113	152 ± 10	137 ± 7
H5-1	eu	129	98	0.759	3	0.33	0.0603 ± 25	0.0218 ± 9	0.1815 ± 113	169 ± 10	139 ± 6
H7-1	eu	1181	770	0.652	27	0.15	0.0486 ± 7	0.0212 ± 9	0.1417 ± 68	135 ± 6	135 ± 6
H6-1	eu	234	157	0.670	6	1.10	0.0506 ± 35	0.0218 ± 9	0.1518 ± 129	143 ± 11	139 ± 6
H8-1	eu	340	404	1.187	9	0.37	0.0543 ± 20	0.0224 ± 10	0.1674 ± 105	157 ± 9	143 ± 7
H13-1	eu	124	180	1.443	3	1.41	0.0509 ± 89	0.0183 ± 8	0.1284 ± 240	123 ± 22	117 ± 5
H14-1	eu	105	34	0.326	2	2.72	0.0361 ± 74	0.0232 ± 8	0.1154 ± 245	111 ± 22	148 ± 5
H15-1	eu	228	169	0.743	5	1.53	0.0489 ± 44	0.0204 ± 10	0.1375 ± 149	131 ± 13	130 ± 7
H1-1	fr	13	47	3.687	0	11.84	0.0121 ± 489	0.0118 ± 16	0.0196 ± 798	20 ± 77	75 ± 10
H9-1	fr	24	31	1.333	0	7.41	0.0483 ± 288	0.0139 ± 9	0.0923 ± 561	90 ± 54	89 ± 6
H11-1	fr	22	74	3.410	1	10.01	0.0634 ± 299	0.0176 ± 13	0.1534 ± 746	145 ± 68	112 ± 8
H10-1	fr-c	543	186	0.343	98	0.03	0.1208 ± 11	0.1711 ± 71	2.85 ± 12	***1968 ± 16***	1018 ± 39
H10-2	fr-r	30	25	0.852	1	6.29	0.0698 ± 232	0.0310 ± 19	0.30 ± 10	***922 ± 895***	197 ± 12
H12-1	fr	723	207	0.287	112	0.05	0.1053 ± 4	0.1534 ± 82	2.23 ± 12	***1719 ± 7***	920 ± 46

Note: eu = euhedral zircons; fr = fragmented zircons; c = core; r = rim. f_{206}(%) is percent of total ^{206}Pb which is non-radiogenic. The italic data are $^{207}Pb/^{206}Pb$ apparent ages.

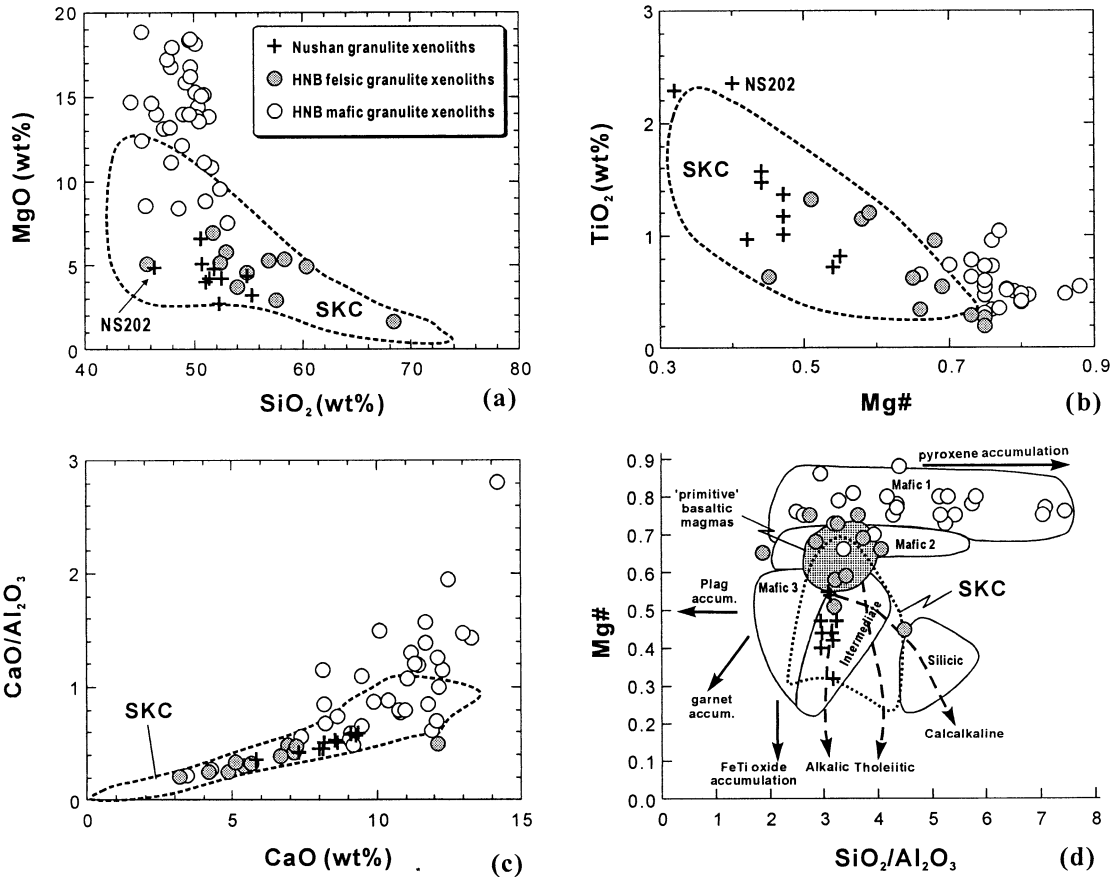

Fig. 2. Major elements diagrams of the Nushan granulite xenoliths. (a) SiO_2 vs. MgO; (b) Mg# vs. TiO_2; (c) CaO vs. CaO/Al_2O_3; (d) Mg# vs. SiO_2/Al_2O_3. Fields for world-wide granulite xenoliths (Mafic1, Mafic2, Mafic3, Intermediate and Silicic) are from Kempton and Harmon (1992) and Kempton et al. (1997); dashed arrows indicate average differentiation trends for alkalic, tholeiitic and calc-alkaline melts, and continuous arrows show generalized direction of compositional change with accumulation of indicated mineral phase; HNB, Hannuoba granulite xenoliths (Liu et al., 2001; Huang et al., 2001).

for trace elements and rare-earth elements (REE) by inductively coupled plasma-mass spectrometry (ICP-MS) at the Guangzhou Institute of Geochemistry, Chinese Academy of Sciences (GIGCAS), using techniques described by Liu et al. (1996) and Xu (2002). Precision for REE and other incompatible elements are estimated to be 5% from the international USGS reference samples BIR-1 and an internal standard (ROA-1). Measured values of standards are generally in good agreement with reference data (Xu, 2002). Duplicate runs gave <10% RSD (relative standard deviation) for most elements analyzed.

Sr-Nd isotopic ratios have been measured on a subset of whole rock samples. The isotopic analyses were carried out using a Micromass Isoprobe Multi-Collector Inductively Coupled Plasma Mass Spectrometry (MC-ICPMS) at GIGCAS. Analyses of standards during the period of analysis are as follows: NBS987 gave $^{87}Sr/^{86}Sr = 0.710243 \pm 14$ (2σ); Shin Etou gave $^{143}Nd/^{144}Nd = 0.512124 \pm 11$ (2σ).

Zircons were separated from two samples (NS214, NS202) using conventional heavy liquid and magnetic techniques and purified by hand-picking under binocular. They are mounted together with the standard zircons (TEM) in epoxy resin. The mount surface was polished to ensure the exposure of grain and then was gold coated. Internal structure of zircons was examined using cathodoluminescence (CL) and back-scattered-electron (BSE) image technique before U-Pb isotopic analyses. The U-Pb analyses were performed using a Sensitive High-Resolution Ion Microprobe (SHRIMP II) at the Institute of Geology, Chinese Academy of Geological Sciences, Beijing, and detailed analytical procedures are similar to those described by Compston et al. (1984) and Williams (1992). The standard TEM zircons (age 417 Ma) of RSES were used in interelement fractionation, and U, Th and Pb concentrations were determined based on the standard Sri Lankan gem zircon SL13, which has a U concentration of 238 ppm corresponding to an age of 572 Ma. Data processing procedures were after PRAWN (Williams et al., 1996), and the ^{204}Pb-based method of common Pb correction was applied. Uncertainties of data points reported in Table 3 and Table 4 are given at $\pm 1\sigma$. The ages quoted in the text are $^{207}Pb/^{206}Pb$ ages or $^{206}Pb/^{238}U$ ages, which are the weighted mean at the 95% confidence level.

5. RESULTS

5.1. Major Elements

The Nushan granulite xenoliths show a basic to intermediate composition with $SiO_2 = 46–56$ wt.% and Mg# ranging from 0.32 to 0.55 (Table 2). Among the samples analyzed, NS202 shows distinctly lower SiO_2, higher TiO_2 and FeO contents. Its relatively high Fe_2O_3 contents (up to 8.96 wt.%) may be due to the high proportion of Fe-Ti oxides. According to the discriminant function (D.F.) proposed by Shaw (1972), most of the Nushan granulite xenoliths have positive D.F. values (Table 2), consistent with an igneous parentage.

Whole rock data show a close affinity of the Nushan gran-

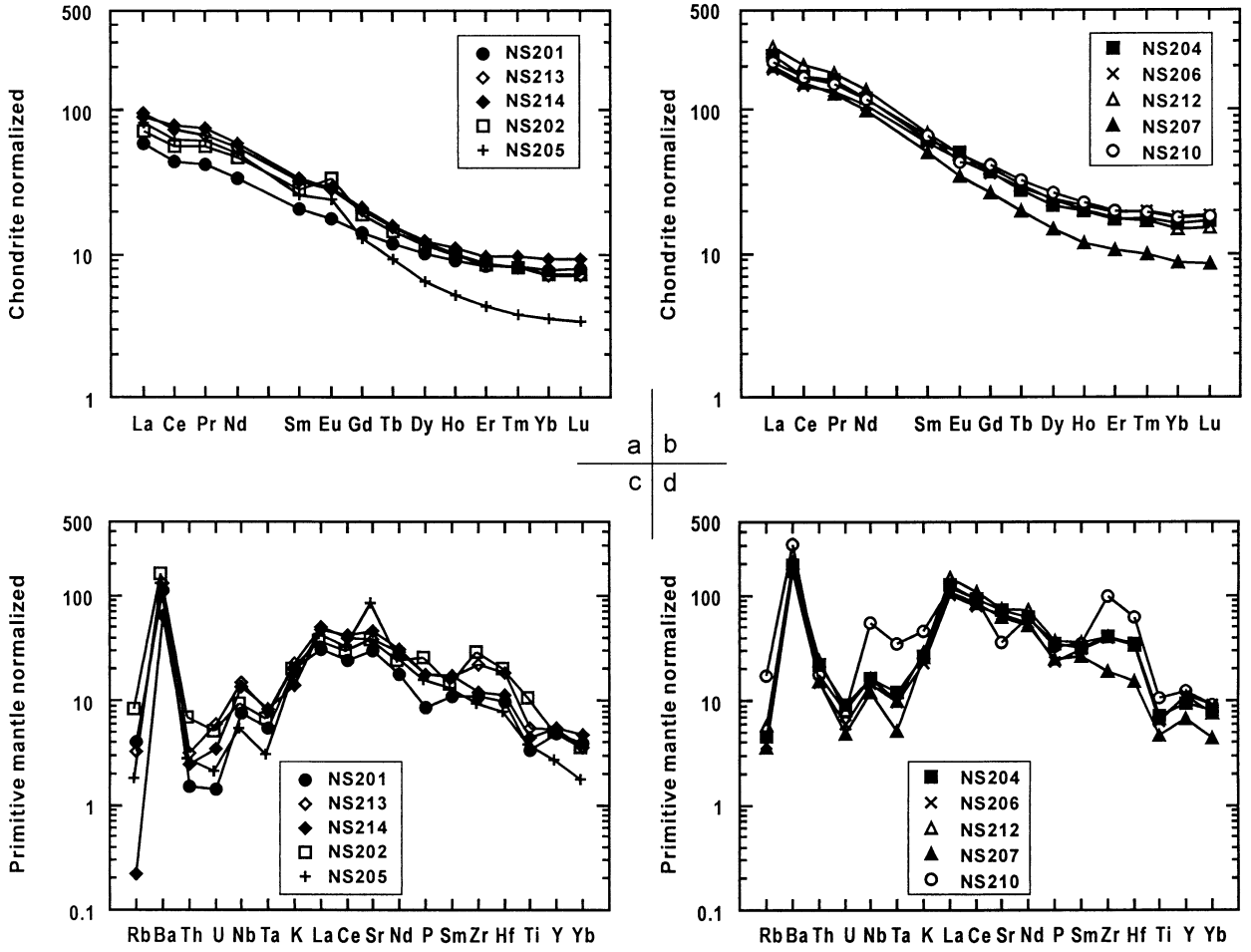

Fig. 3. Chondrite normalized REE patterns (a and b) and primitive mantle-normalized incompatible trace element diagrams (c and d) for Nushan granulite xenoliths. Normalizing values of Sun and McDonough (1989).

ulite xenoliths with the granulite terrains, and a remarkable distinction from the Hannuoba mafic granulites. This is obvious from Figure 2, in which the Nushan granulite xenoliths show similar TiO_2, SiO_2 contents, Mg# values and CaO/Al_2O_3 ratios as the granulite terrains of the SKC, but have markedly lower MgO contents, Mg# values and CaO/Al_2O_3 ratios, and higher TiO_2 contents (0.72–2.35 wt.%) than the Hannuoba mafic granulite xenoliths (Fig. 2). In the Mg# vs. SiO_2/Al_2O_3 diagram (Kempton and Harmon, 1992; Kempton et al., 1997), the Nushan granulite xenoliths are plotted within the field of intermediate compositions, thereby resembling the Archean granulite terrains from the SKC (Fig. 2d), whereas the Hannuoba granulite xenoliths fall into the fields of mafic rocks. Figure 2d shows that the Hannuoba granulites compositionally vary along the trend of pyroxene accumulation, whereas the Nushan samples plot on the fractionation trend of alkali basaltic magma. TiO_2 contents negatively correlate with Mg# values (Fig. 2b), and CaO/Al_2O_3 ratios decrease with CaO contents (Fig. 2c).

5.2. Trace Elements

In terms of ΣREE contents, two groups of xenoliths can be distinguished. For example, NS201, NS202, NS205, NS213 and NS214 are relatively low in ΣREE (<200 ppm, Table 2) with HREE contents being less than 10 × chondrite (Fig. 3a). In contrast, NS204, NS206, NS207, NS210 and NS212 are characterized by high ΣREE contents (>350 ppm, Table 2), and HREE contents mainly about 20 × chondrite (Fig. 3b). The different REE contents are apparently dependent on the presence of apatite. Apatites are common in thin sections of the xenoliths with high ΣREE, and the REE abundances of the xenoliths increase with P_2O_5 except for NS202 (Fig. 4a). Both P_2O_5 and REE contents all decrease with Mg# (Fig. 4b, c), indicating a trend of fractional crystallization. Except for different ΣREE, two groups show similar REE patterns which are characterized by enrichment of LREE relative to HREE with La_N/Yb_N = 7.5–23 (Fig. 3a, b; Table 2). Most of the samples have no obvious Eu anomaly, but NS202 and NS205 have positive Eu anomalies (Fig. 3a).

The Nushan granulites are all characterized by enrichment of Ba, K, Zr and Hf and by depletion of Rb, Th, U, Nb, Ta and Ti (Fig. 3c, d). Positive Eu anomalies in NS205 and NS202 are corroborated with the positive Eu anomalies, reflecting the effect of plagioclase accumulation. The Nushan granulite xenoliths contain very low Rb (0.14–11.2 ppm), U and Th contents

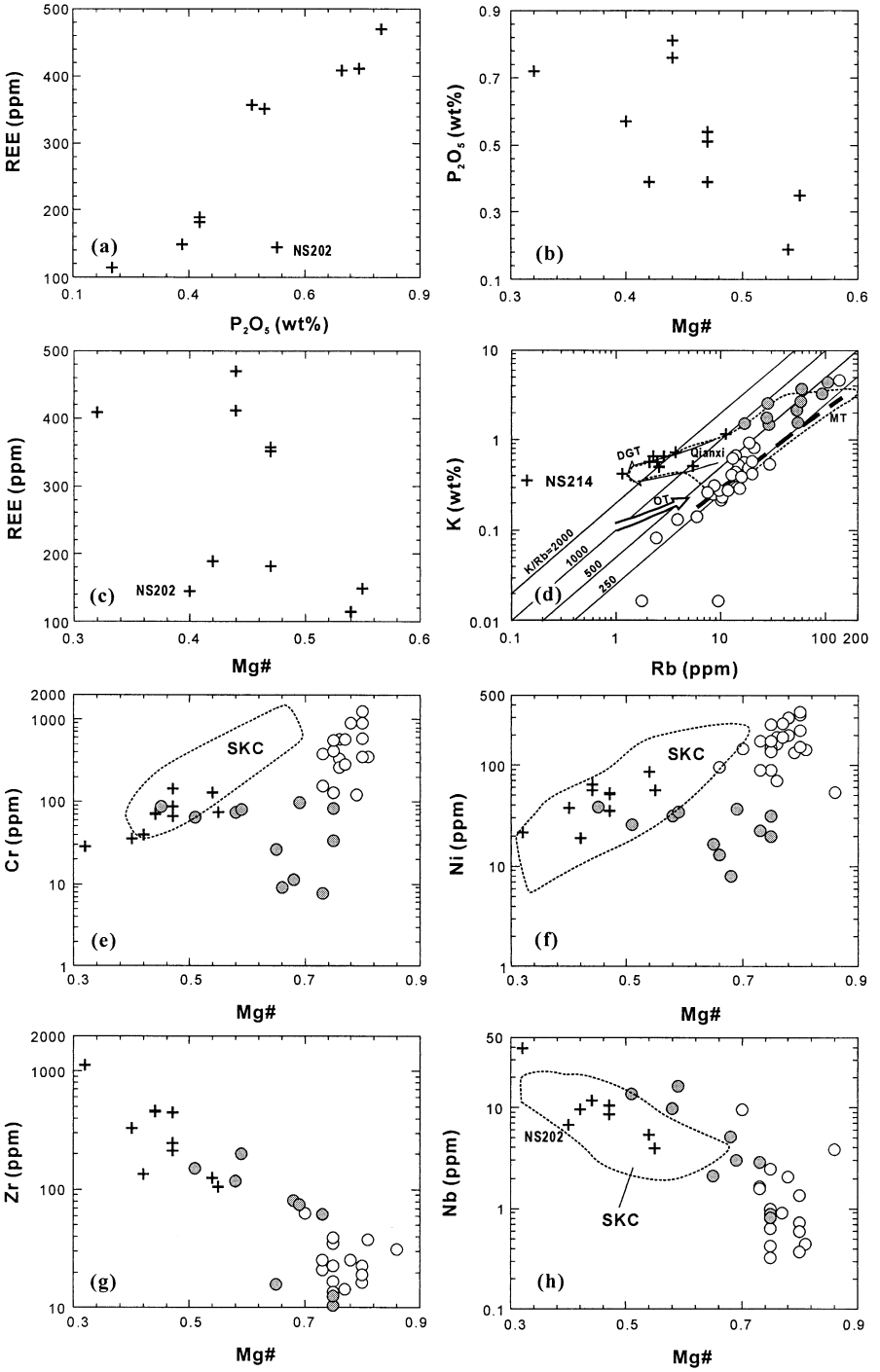

Fig. 4. Trace elements diagrams of the Nushan granulite xenoliths. (a) P_2O_5 vs. REE; (b) Mg# vs. P_2O_5; (c) Mg# vs. REE; (d) Rb vs. K; (e) Mg# vs. Cr (f) Mg# vs. Ni; (g) Mg# vs. Zr; (h) Mg# vs. Nb. Both legends and source of data are same as Figure 2. granulite terrains of the Sino-Korean Craton (Huang et al., 2001; Jahn and Zhang, 1984).

(Table 2). Similar low Rb, Th and U contents are observed in the Archean Qianxi granulites (Jahn and Zhang, 1984; Jahn, 1990). The depletion of these large ion lithophile elements (LILE) could be related to granulite-facies metamorphism (Moorbath and Taylor, 1986). The Nushan granulite xenoliths have relatively constant K/Ba ratios (4.4–7.8, Table 2) and high Ba contents (458–2123 ppm, Table 2), suggesting that Ba contents may not have been significantly affected by the metamorphism. Similar to the Archean granulite terrains of the SKC, high Ba contents may reflect a primary characteristic of the protoliths (Shen et al., 1994). Additionally, variable Rb depletion relative to K of the Nushan granulites follows the

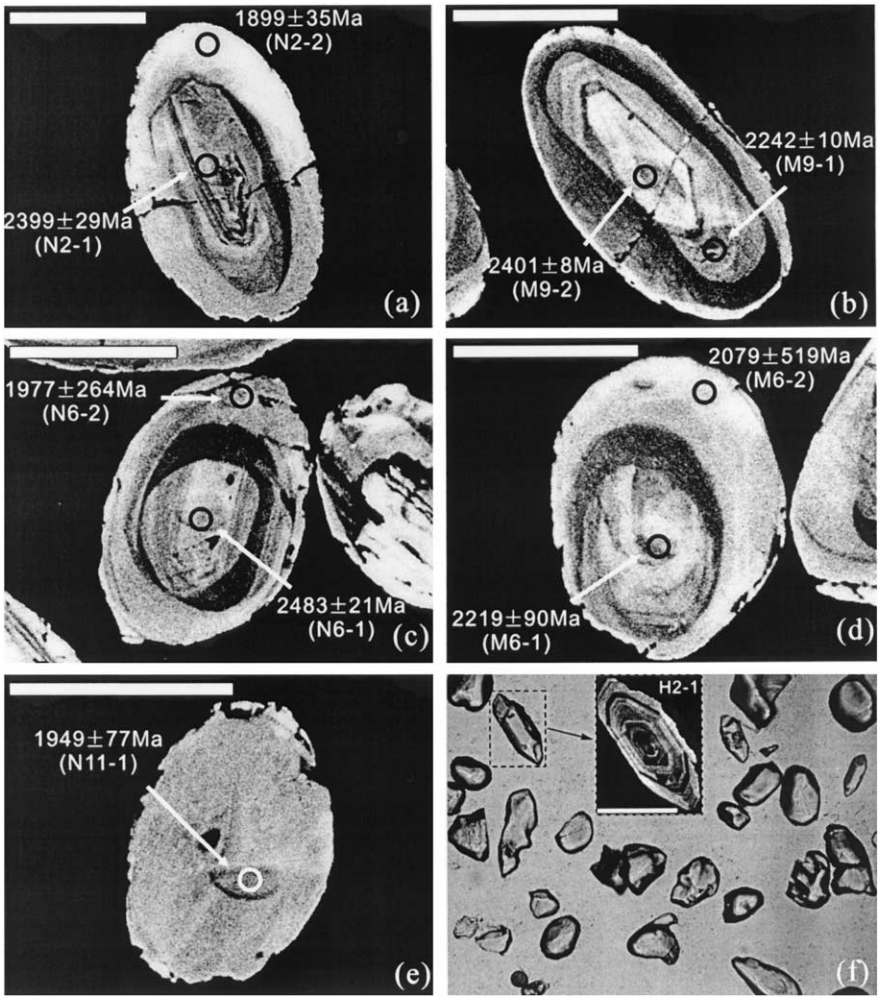

Fig. 5. (a–e) Selected cathodoluminescence (CL) images of zircons in NS214; (f) Morphometrics and selected CL image of zircons in NS202. The numbers refer to the $^{207}Pb/^{206}Pb$ ages of the analytical spots in Table 2. The length of scale bar is 100 μm

trend defined by the Archean Qianxi granulites (Jahn, 1990), but differs from that of the Hannuoba granulites which is similar to the trend for continental granitoids (Fig. 4d).

Cr, Ni, Nb and Ta contents in the Nushan samples are similar to those in the granulite terrains of the SKC and some Hannuoba intermediate granulite xenoliths, but are significantly different from those in the mafic granulite xenoliths from Hannuoba (Fig. 4e, f, h). The positive correlations between Cr/Ni and Mg# (Fig. 4e, f) suggest the fractionation of spinel and olivine. Furthermore, Zr, Hf, Nb and Ta all decrease with Mg# (Fig. 4g, h), indicating a role of fractional crystallization.

5.3. Zircon SHRIMP U-Pb Age

Zircons from intermediate sample of NS214 are dominantly subeuhedral columnar crystals and subordinately slightly rounded. Cathodoluminescence (CL) images show that most zircons are composed of core and rim (Fig. 5a–d). The cores commonly show micro-scale oscillatory zoning, suggesting an igneous origin. The rims, characterized by unzoned overgrowths, are interpreted as results of metamorphic recrystallization. A small number of rounded zircons show homogeneous CL images (Fig. 5e) and are interpreted to be results of granulite-facies metamorphism or strong metamorphic recrystallization. Thirty spots on 23 zircons from NS214 have been analyzed for U-Th-Pb (Table 3). While the spots M3-1 and N11-1 yield concordant $^{207}Pb/^{206}Pb$ ages of 2282 Ma and 1949 Ma, respectively, most of the results are discordant (Fig. 6a, Table 3) suggesting an extensive Pb-loss. However, regression of all the analyses of metamorphic zircons including overgrowth and patches (i.e., spots of N2-2, N4–1, N6-2, N7-1, N8-2, N11-1, N13-1, N14-1, M2-1, M6-2, M7-1) yields an upper intercept age of 1915 $\pm$ 27 Ma (MSWD = 1.01) (Fig. 6a). This age is interpreted as the granulite metamorphism age. Recently, a zircon U-Pb age of 1960 $\pm$ 67 Ma has been obtained for the granitic gneiss of Mazhengkou (Fig. 1), suggesting that the Precambrian crystalline basement in Eastern Shandong Province has experienced a very strong thermotectonic event during the late Paleoproterozoic (Lu, 1998). The Nushan granulite-facies metamorphism age of 1915 $\pm$ 27 Ma is compatible with this event. Other 19 analyses on the igneous

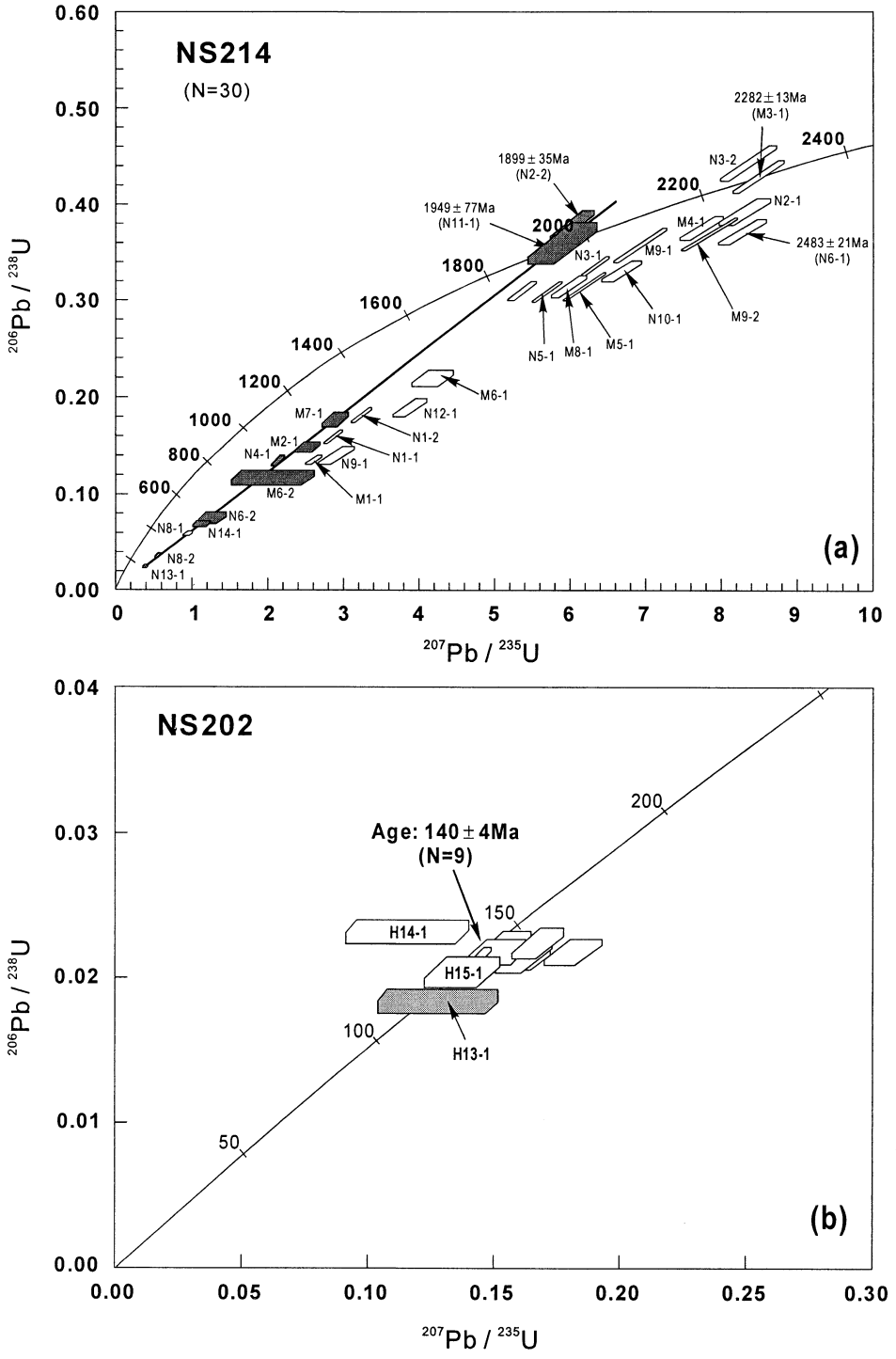

Fig. 6. U-Pb zircon Concordia diagram for (a) an intermediate granulite xenolith (NS214) and (b) a mafic granulite xenolith (NS202). Most of the analyses in (a) are discordant. The metamorphic zircons (filled symbols) define a linear array that gives an upper intercept age of 1915 ± 27 Ma (MSWD = 1.01), whereas the magmatic zircons (open symbols) do not define a linear array. Data in (b) are concordant or near-concordant, and 9 analyses yield a weighted mean $^{207}Pb/^{235}U$ age of 140 ± 4 Ma.

cores of zircons do not define any linear array (Fig. 6a), but the concordant $^{207}Pb/^{206}Pb$ age of 2282 ± 13 Ma on Spot M3-1 (Fig. 6a, Table 3) suggests that the protolith of the Nushan granulite xenoliths may have been formed at 2.2 Ga ago. An even older age (i.e., late Archean) can be inferred because analyses on Spot N6-1 yield 2483 ± 21 Ma. However, it is

Table 5. Sr and Nd isotope compositions of the Nushan granulite xenoliths.

Sample	$^{87}Rb/^{86}Sr$	$^{87}Sr/^{86}Sr$ (2σ)	$(^{87}Sr/^{86}Sr)_i$	$^{147}Sm/^{144}Nd$	$^{143}Nd/^{144}Nd$ (2σ)	T_{CHUR}(Ga)†	ε_{Nd} (140 Ma)	ε_{Nd} (2.5Ga)
NS201	0.0115	0.707117 ± 18	0.7067	0.121936	0.511371 ± 9	2.57	−23.4	−0.7
NS202	0.0192	0.706957 ± 17	0.7063	0.115821	0.511143 ± 11	2.80	−27.7	−3.2
NS204	0.0053	0.704077 ± 20	0.7039	0.100239	0.511146 ± 6	2.35	−27.4	1.9
NS205	0.0019	0.704041 ± 14	0.7040	0.102403	0.510812 ± 10	2.93	−33.9	−5.3
NS206	0.0051	0.704148 ± 17	0.7040	0.109272	0.511158 ± 6	2.57	−27.3	−0.8
NS207	0.0049	0.705898 ± 16	0.7057	0.101330	0.510941 ± 6	2.70	−31.4	−2.5
NS210	0.0429	0.707011 ± 18	0.7055	0.111108	0.511120 ± 15	2.69	−28.1	−2.1
NS212	0.0066	0.704102 ± 15	0.7039	0.098825	0.511117 ± 7	2.36	−27.9	1.8
NS213	0.0074	0.704891 ± 16	0.7046	0.114493	0.511093 ± 8	2.85	−28.7	−3.7
NS214	0.0004	0.705090 ± 23	0.7050	0.114342	0.510786 ± 10	3.40	−34.7	−9.7

$^{87}Rb/^{86}Sr$ and $^{147}Sm/^{144}Nd$ are calculated using whole-rock Rb, Sr, Sm and Nd contents in Table 4. $(^{87}Sr/^{86}Sr)_i$ is the apparent initial ratio for 2.5 Ga calculated based on the observed Rb/Sr value. $^{143}Nd/^{144}Nd$ ratios were normalized using a $^{146}Nd/^{144}Nd$ value of 0.7219 and were further adjusted to the La Jolla Nd standard (0.511860).

† The following values have been used in the calculation: $(^{143}Nd/^{144}Nd)^0_{CHUR} = 0.512638$, $(^{147}Sm/^{144}Nd)^0_{CHUR} = 0.1967$.

noticeable that the $^{207}Pb/^{206}Pb$ ages on the igneous cores define a chord from 2.5 Ga to the origin of the data and show a shift toward the 1.9 Ga chord (Fig. 6a). It is quite possible that the 2.5 Ga and 1.9 Ga chords point to real events such as magmatism and granulite-facies metamorphism, respectively. The concordant $^{207}Pb/^{206}Pb$ age of 2282 Ma may not really represent an age. It could have resulted from disturbance of granulite-facies metamorphism at 1.9 Ga.

Zircons from mafic sample of NS202 are dominantly fragmented or slightly rounded crystals (Fig. 5f). However, a few are euhedral with well-developed tetragonal dipyramids. The oscillatory zonings in these euhedral zircons (Fig. 5f) suggest an igneous origin. Analyses on fragmented zircons failed to yield meaningful results because of very high f_{206} (Spots H1-1, H9-1, H10-2, H11-1; Table 4) or gave the discordant ages (Spots H10-1, H12-1; Table 4), which may be results of strong disturbance of thermo-tectonic events in recent times. However, analyses of ten euhedral zircons (Table 4) yield concordant or near concordant ages. A weighted mean $^{206}Pb/^{238}U$ age of 140 ± 4 Ma is obtained based on all but one analyses (Fig. 3b). The analysis H13-1 yields a slightly younger concordant $^{206}Pb/^{238}U$ age of 117 ± 5 Ma. These ages suggest that parts of the Nushan lower crust may have been formed during the Mesozoic.

5.4. Sr-Nd Isotopes

Measured $^{143}Nd/^{144}Nd$ ratios for the Nushan granulite xenoliths range between 0.5108 and 0.5114. The single-stage chondritic Nd model ages (T_{CHUR}, Table 5) range from 2.4 to 3.4 Ga (mostly between 2.4 Ga and 2.9 Ga). The initial ε_{Nd} at 2.5 Ga vary between −9.7 and 1.9 (Table 5), within the range of Archean rocks in the SKC (Fig. 7a). The calculated $^{143}Nd/^{144}Nd$ ratios of the Nushan granulites at 140 Ma are significantly lower than those of the Hannuoba granulites (Fig. 7b).

The measured $^{87}Sr/^{86}Sr$ of the Nushan granulite xenoliths range between 0.7040−0.7071 (Table 5). Based on the observed Rb/Sr ratios, the apparent initial $^{87}Sr/^{86}Sr$ at 2.5 Ga

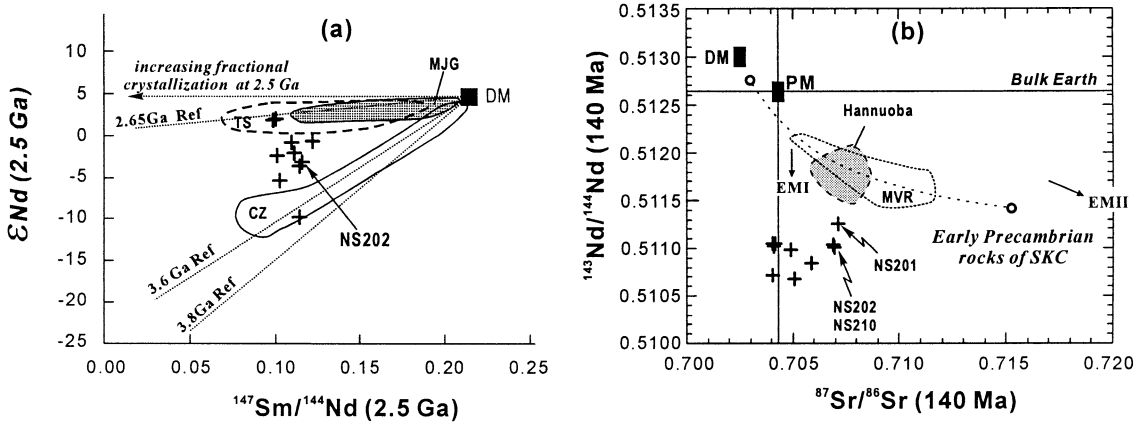

Fig. 7. (a) ε_{Nd} (*2.5Ga*) vs. $^{147}Sm/^{146}Nd$ plots of the Nushan granulite xenoliths; (b) Correlation between Sr and Nd isotopic at 140 Ma for the Nushan granulites, both Hannuoba granulites and Mesozoic volcanic rocks of Eastern China show the EMI affinity in protolith source. Abbreviations and source of data: TS, Taishan complex (Jahn et al., 1988); MJG, Mangjinggou high-P granulite terrain (Guo et al., 1994); CZ, Caozhuang amphibolites (Jahn et al., 1987); MVR, Mesozoic volcanic rocks of Eastern China (Wang et al., 1996); Hannuoba granulites (Zhou et al., 2002).

Table 6. The mineral compositions (wt %) of Nushan granulite xenoliths.

	NS201			NS202				NS203			NS204			NS205			NS206			
Sample					Opx-	Opx-											Cpx-	Cpx-		
Mineral	Cpx	Opx	Pl	Cpx	c	r	Pl	Cpx	Opx	Pl	Cpx	Opx	Pl	Cpx	Opx	Pl	1	2	Opx	Pl
SiO_2	49.74	51.00	55.27	50.65	52.70	52.20	56.97	51.39	50.60	58.59	51.08	50.30	58.56	51.64	51.77	58.78	50.84	50.80	51.61	58.19
TiO_2	0.35	0.00	0.00	0.35	0.08	0.06	0.00	0.21	0.09	0.01	0.23	0.05	0.01	0.25	0.11	0.00	0.30	0.31	0.05	0.00
Al_2O_3	4.13	3.19	28.17	3.79	1.86	2.21	28.06	2.39	1.80	25.92	3.48	2.68	26.30	2.87	1.79	26.08	3.71	3.78	2.19	26.43
Cr_2O_3	0.18	0.11	0.64	0.04	0.04	0.08	0.04	0.00	0.01	0.07	0.00	0.07	0.47	0.00	0.08	0.06	0.10	0.32	0.00	0.74
FeO	9.89	23.29	0.14	11.15	25.85	23.62	0.17	11.24	26.58	0.13	10.83	25.84	0.08	11.51	24.42	0.14	10.85	9.21	24.78	0.20
MnO	0.16	0.23	0.00	0.20	0.38	0.35	0.04	0.31	0.53	0.03	0.04	0.35	0.02	0.34	0.40	0.05	0.11	0.31	0.46	0.02
MgO	12.43	21.33	0.01	12.41	19.13	21.31	0.02	11.79	19.61	0.00	12.22	19.87	0.01	12.13	20.25	0.00	12.43	12.29	20.02	0.01
CaO	20.83	0.54	9.99	21.66	0.43	0.41	7.82	21.17	0.61	7.13	21.75	0.47	7.67	21.11	0.64	7.74	20.89	21.38	0.44	7.48
Na_2O	0.57	0.02	5.10	0.47	0.07	0.09	6.17	0.60	0.04	7.53	0.74	0.11	6.22	0.56	0.11	6.60	0.78	0.77	0.07	6.11
K_2O	0.00	0.00	0.58	0.01	0.01	0.03	0.48	0.02	0.00	0.57	0.01	0.00	0.73	0.02	0.00	0.80	0.03	0.01	0.02	0.52
Total	98.28	99.71	99.90	100.73	100.55	100.36	99.77	99.12	99.87	99.98	100.38	99.74	100.07	100.43	99.57	100.25	100.04	99.18	99.64	99.70
Mg#	0.69	0.62		0.66	0.57	0.62		0.65	0.57		0.67	0.58		0.65	0.60		0.65	0.70	0.59	
Wo(An)	45.4	1.1	50.2	45.5	0.9	0.8	40.0	45.7	1.2	33.3	46.1	1.0	38.7	44.9	1.3	37.5	41.5	46.8	0.9	39.1
En(Ab)	37.7	61.3	46.4	36.2	56.3	61.1	57.1	35.4	56.1	63.6	36.0	57.3	56.9	35.9	58.9	57.9	38.0	37.4	58.5	57.7
Fs(Or)	16.8	37.6	3.5	18.3	42.7	38.0	2.9	18.9	42.7	3.2	17.9	41.8	4.4	19.1	39.8	4.6	20.5	15.7	40.6	3.2

	NS207			NS210			NS212			NS213			NS214			NS217		
Sample Mineral	Cpx	Opx	Pl	Cpx	Opx	Pl	Cpx	Opx	Pl	Cpx	Opx	Pl	Cpx	Opx	Pl	Cpx	Opx	Pl
SiO_2	50.88	51.31	57.76	51.55	50.85	59.07	50.21	52.00	58.99	51.54	52.54	59.48	50.56	51.56	57.63	51.06	51.12	59.98
TiO_2	0.19	0.06	0.03	0.19	0.07	0.01	0.26	0.08	0.00	0.16	0.03	0.01	0.25	0.05	0.00	0.37	0.06	0.00
Al_2O_3	2.79	1.81	26.20	2.34	1.26	24.74	3.26	1.77	26.05	2.42	1.37	26.47	2.39	1.66	26.26	2.09	1.20	24.91
Cr_2O_3	0.00	0.00	0.00	0.24	0.03	0.67	0.04	0.01	0.19	0.05	0.02	0.06	0.04	0.00	0.01	0.00	0.00	0.00
FeO	10.68	25.42	0.11	12.08	30.06	0.08	11.15	24.75	0.08	10.12	25.36	0.02	10.23	24.49	0.04	10.16	25.42	0.12
MnO	0.43	0.72	0.00	0.18	0.30	0.03	0.17	0.33	0.00	0.09	0.33	0.00	0.15	0.48	0.00	0.08	0.00	0.04
MgO	12.23	20.60	0.00	11.12	16.58	0.01	11.92	20.04	0.00	12.25	20.60	0.00	12.44	20.69	0.00	12.62	20.92	0.02
CaO	21.85	0.55	8.51	21.83	0.62	6.73	21.44	0.49	7.61	21.21	0.51	7.11	21.99	0.53	7.77	22.40	0.43	7.35
Na_2O	0.57	0.00	5.94	0.66	0.10	7.14	0.68	0.00	6.33	0.54	0.03	7.16	0.61	0.01	6.81	0.38	0.00	7.96
K_2O	0.00	0.01	0.55	0.00	0.00	0.65	0.01	0.01	0.73	0.00	0.02	0.41	0.00	0.00	0.51	0.01	0.00	0.18
Total	99.62	100.48	99.10	100.19	99.87	99.13	99.14	99.48	99.98	98.38	100.81	100.72	98.66	99.47	99.03	99.17	99.15	100.56
Mg#	0.67	0.59		0.62	0.50		0.66	0.59		0.68	0.59		0.68	0.60		0.69	0.59	
Wo(An)	46.3	1.1	42.8	46.7	1.3	33.0	45.9	1.0	38.2	46.0	1.0	34.6	46.5	1.1	37.5	46.8	0.9	33.4
En(Ab)	36.0	58.4	54.0	33.1	48.9	63.3	35.5	58.5	57.5	36.9	58.5	63.0	36.6	59.4	59.5	36.7	59.0	65.6
Fs(Or)	17.7	40.4	3.3	20.2	49.8	3.8	18.6	40.5	4.4	17.1	40.4	2.4	16.9	39.5	2.9	16.6	40.2	1.0

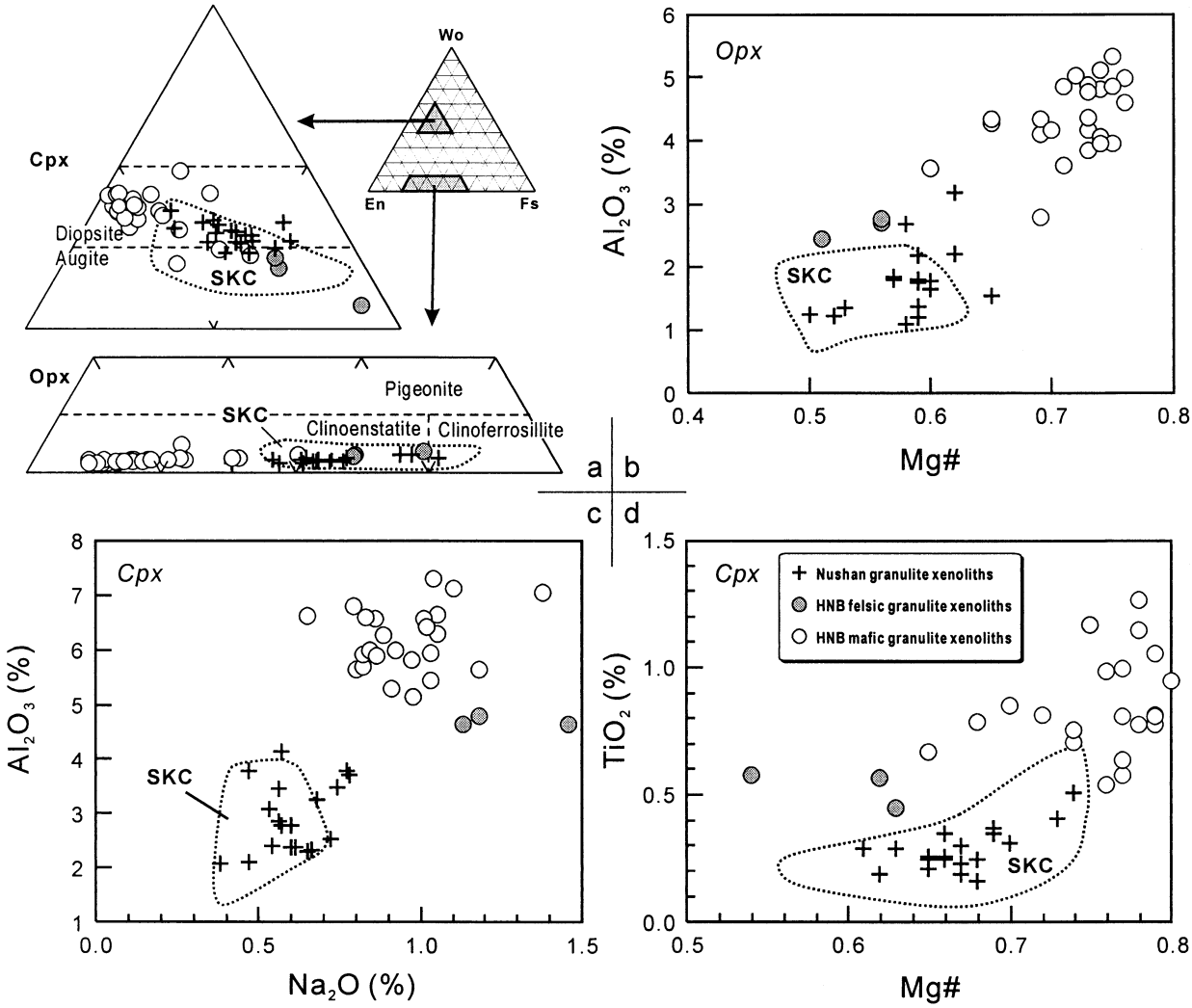

Fig. 8. Compositional characteristics of orthopyroxenes and clinopyroxenes in the Nushan granulite xenoliths, source of data: this work and Xu et al. (1998). SKC, Sino-Korean craton (Guo et al., 1998; Liu et al., 1997); HNB, Hannuoba granulite xenoliths (Chen et al., 2001).

range from 0.7039 to 0.7067 (Table 5). However, as discussed previously, Rb contents in the Nushan granulites may have been significantly lowered by granulite metamorphism, it is therefore not easy to estimate the initial Sr isotopic ratios for these samples. The measured $^{87}Sr/^{86}Sr$ ratios can be considered as the maximum estimates of the initial ratios.

5.5. Mineral Chemistry

Plagioclase composition in the Nushan granulite xenoliths varies from andesine to labradorite ($An_{33\sim50}Ab_{46\sim66}Or_{1\sim5}$). The Mg# values of orthopyroxenes range from 0.50 to 0.62 and end-members of orthopyroxenes are $Wo_{\sim1}En_{49\sim61}Fs_{38\sim50}$ (Table 6, Fig. 8a). Bhattacharyya (1971) suggested that orthopyroxenes with MgO + FeO + Fe_2O_3 + $0.775Al_2O_3$ greater than 44.3 are metamorphic in origin, whereas orthopyroxenes with the discrimination values less than 44.3 are likely magmatic in origin. For orthopyroxene from the Nushan granulite xenoliths, this value varies from 46.1 to 48.4, which suggests a metamorphic origin. However, the relatively higher amount of wollastonite (Wo = 0.8 ~ 1.3%, Table 6) implies that these orthopyroxenes may have resulted from recrystallization of former magmatic minerals (Rietmeijer, 1983). The end-members of clinopyroxenes are $Wo_{42-47}En_{33-38}Fs_{17-21}$ (Fig. 8a), and Mg# values vary in the range of 0.62–0.70 (Table 6). As shown in Figure 8, the Nushan pyroxenes are compositionally similar to those from the granulite terrains in the SKC, but significantly different from those of the Hannuoba xenoliths. Specifically, both orthopyroxene and clinopyroxene of the Nushan granulites have lower Mg# values than the counterparts from Hannuoba. Moreover, the Nushan granulite xenoliths show lower Na_2O, Al_2O_3 and TiO_2 in clinopyroxenes (Fig. 8c, d), and lower Al_2O_3 but higher FeO in orthopyroxenes, when compared with the Hannuoba granulites (Fig. 8a, b).

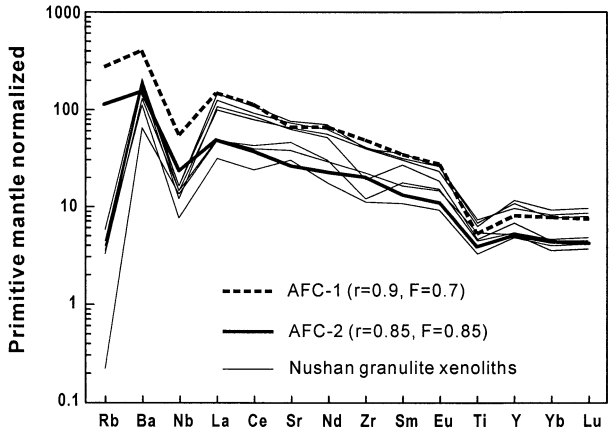

Fig. 9. AFC modeling of trace elements of the Nushan granulite xenoliths. Mode of crystallizing phase: AFC-1: $Cpx_{0.45}Opx_{0.3}Pl_{0.02}Ol_{0.1}Grt_{0.03}Sp_{0.05}Il_{0.03}Mt_{0.02}$; AFC-2: $Cpx_{0.4}Opx_{0.2}Ol_{0.1}Grt_{0.1}Sp_{0.05}Il_{0.05}Mt_{0.05}Apt_{0.05}$. Average composition of late Archean mafic volcanic rocks (Liu et al., 1998) and average composition of the lower crust of SKC (Gao et al., 1998a) are used as the primary magma and contaminant, respectively. "r" - mass of assimilate to cumulate, "F" - melt fraction. Partition coefficients used in calculations as in Kempton et al. (1997). AFC model equations from DePaolo (1981). Normalizing values from Sun and McDonough (1989).

6. DISCUSSION

6.1. Petrogenesis

The remarkably different U-Pb ages imply the existence of two xenolith populations at Nushan, which are characterized by different geochemical features. A number of comparison diagrams (Figs. 2, 4, 8) show that the Nushan granulites are compositionally similar to the Archean granulite terrains exposed in the SKC and some felsic granulite xenoliths from Hannuoba, but differ significantly from the Hannuoba mafic granulite xenoliths. The Nd model age relative to the CHUR (T_{CHUR} = 2.4–3.4 Ga, Table 5) also implies a provenance from very old reservoir. This is supported by the zircon SHRIMP U-Pb dating of intermediate sample NS214 that the protoliths of the Nushan intermediate granulites were likely formed at ca. 2.5 Ga and then subjected to granulite-facies metamorphism at 1.9 Ga. The overall intermediate compositions of the Nushan granulites could have resulted from assimilation-fractionation-crystallization (AFC) of a mafic basalt precursor. For instance, the positive correlation between CaO/Al_2O_3 and CaO (Fig. 2c) implies segregation of clinopyroxene. Fractionation of olivine and spinel is suggested by the positive correlation between Ni and Cr and Mg#. Unlike the Hannuoba granulites which compositionally vary along the trend of pyroxene accumulation, the Nushan samples form a trend that is similar to the fractionation trend of alkali basaltic magma (Fig. 2d), which is consistent with crystallization of the Nushan granulite protoliths as solidified melts and not as cumulates. The extremely negative ε_{Nd} values of most Nushan granulite xenoliths, together with the widespread HFSE depletion observed in incompatible element patterns (Fig. 3c, d), suggest the role of crustal contamination in magma genesis or the remelting of older continental crust. The latter alternative is not consistent with basic to intermediate compositions of the Nushan granulites. Trace element modeling shows that the Nushan granulite xenoliths can be simulated by 10−40% assimilation-fractional crystallization (AFC)

Table 7. Equilibrium temperature, pressure and calculated P-wave velocity for the Nushan granulite xenoliths.

Sample	T1 (°C)	T2 (°C)	P (kbar)	Depth (km)	V_1 (km s^{-1})	V_2 (km s^{-1})	V_3 (km s^{-1})
NS201	874	899	9.1	30	6.87	6.82	6.99
NS202c	848	887	8.7	29	6.90	6.86	7.02
NS202r	855	877	8.6				
NS203	830	851	6.5	28	6.83	6.79	6.95
NS204	834	853	8.7	29	6.88	6.83	7.00
NS205	841	865	7.6	25	6.69	6.65	6.81
NS206	860	896	9.5	31	6.87	6.83	6.99
NS207	821	831	7.6	25	6.72	6.68	6.84
NS210	779	804	6.4	21	6.69	6.64	6.81
NS212	820	838	7.8	26	6.79	6.74	6.91
NS213	839	865	6.7	22	6.81	6.77	6.93
NS214	804	809	4.8	~20	6.67	6.62	6.79
NS217	813	819	4.5	~20	6.58	6.53	6.70
Nu8902	862	874	7.6	25	6.72	6.68	6.84
Nu8903	806	836	6.2	20	6.81	6.76	6.93
Nu9518	826	820	7.3	24			
Nu9521	809	843	7.2	24			
Nu9523	825	845	6.2	20			

T1 and T2 are calculated by using two-pyroxenites thermometer of Wood and Banno (1973) and Wells (1977), respectively. P is calculated by using the Eq. (7) in McCarthy & Patiño Douce (1998). The equilibrium P-T of NS206 are calculated using the composition of cpx-1 in Table 2; Mineral compositions of samples Nu8902, Nu8903, Nu9518, Nu9521, Nu9523 are from Xu et al. (1998), Mineral modes of Nu8902 and Nu8903 are from Zhou et al. (1992).

V_1 represents calculated V_p based on modal composition of minerals and single crystal velocities at room pressure and temperature (Gebrande, 1982). V_2 indicates velocities corrected to the depth of 30 km using the average present-day Nushan lower crustal temperature of 600°C, and can be really compared with observed lower crustal velocities at Nushan. V_3 is the velocities corrected to room temperature and 600MPa for purpose of comparison with other locations. The correction follows the method of Rudnick and Fountain (1995), which is based on the common pressure (2×10^{-4} km s^{-1} MPa^{-1}) and temperature (-4×10^{-4} km s^{-1} C^{-1}) coefficients of V_P for crustal rocks and uses the generalized geotherms of Chapman and Furlong (1992).

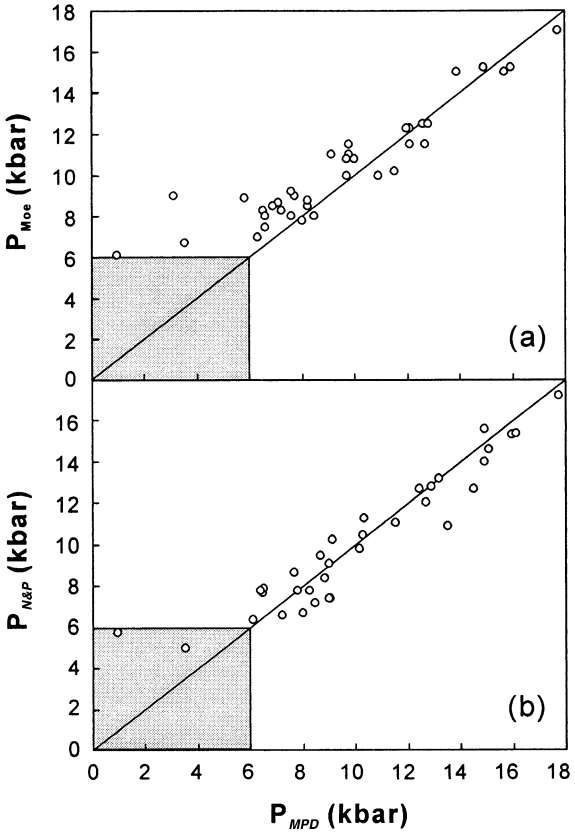

Fig. 10. Comparison of pressures estimated for garnet-bearing granulite using different geobarometers. P_{MPD}, P_{Moe} and $P_{N\&P}$ are the pressures calculated by McCarthy and Patiño Douce (1998), Moecher et al. (1988) and Newton and Perkins (1982) geobarometers, respectively. Source of Data: Yamamoto (1993), Stosch et al. (1995), Ma and Wang (1994) and McCarthy and Patiño Douce (1998).

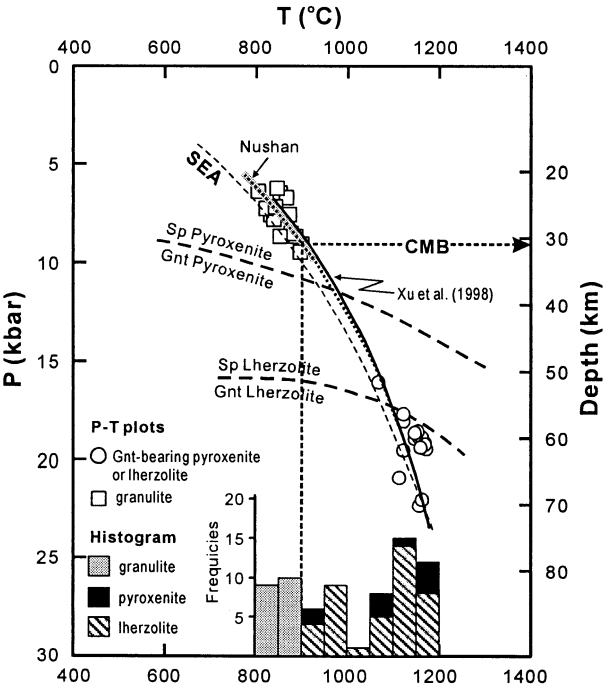

Fig. 11. Nushan geotherm for the lower crust and upper mantle. Histogram for the temperatures of granulites, pyroxenites and lherzolites. Upper mantle geotherm and data of pyroxenites and lherzoilites from Xu et al. (1998); SEA – geotherm for Southeastern Australia (O'Reilly and Griffin, 1985).

of different fractionating assemblages assuming the composition of Archean mafic volcanics as parental magma and the average lower crust of SKC as contaminant (Fig. 9; Huang and Xu, 2002).

The compositional resemblance of the Nushan granulites to the exposed Archean terrains raises the possibility that these xenoliths may come from lower crustal granulites emplaced at shallow level by tectonic processes and eventually sampled by Quaternary basalts. However, at Nushan, granulites are closely associated with abundant mantle xenoliths. The mineral phases (e.g., amphibole) typical of retrograded metamorphism in granulite terrains are absent in the Nushan xenoliths. These observations strongly suggest that the Nushan xenoliths actually represent fragment of the present-day lower crust beneath Nushan, which is mainly composed of the old crystalline basement.

This old lower crust may have been affected by later thermal events, as judged from the ubiquitous lead loss of zircons of the intermediate sample NS214 (Fig. 6a). The weight mean age of 140 ± 4 Ma for the sample NS202 is comparable with those obtained for the granulite xenoliths from Hannuoba (Fan and Liu, 1996; Liu et al., 2001). This age can be interpreted as the time of basaltic underplating during the widespread Mesozoic thermotectonic reactivation of the SKC (Menzies et al., 1993; Griffin et al., 1998; Xu, 2001). The "young" age of NS202 is corroborated with the peculiar composition of this sample. While whole-rock composition of NS202 has some affinities with that of other xenoliths (e.g., LREE-enrichment, LILE contents), but is characterized by distinctly lower SiO_2, ΣREE

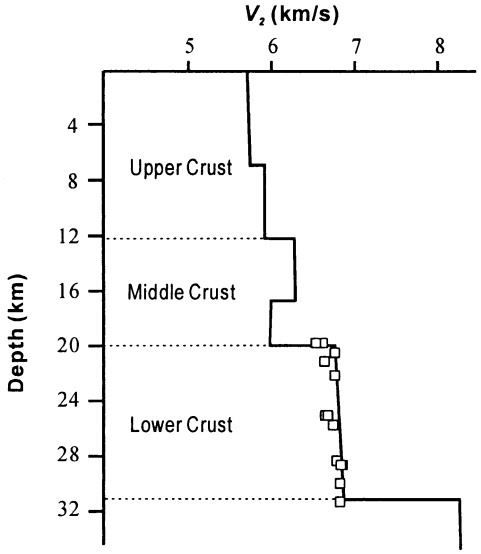

Fig. 12. Seismic velocities (V2) of the Nushan granulite xenoliths (open squares) and seismic velocity structure on Line HQ-13 (Chen, 1988).

Table 8. Estimates of the Lower crustal composition based on the Nushan granulite xenoliths.

	Nushan	HNB	GSKC	CSKC	CYC	GWC	R&F
SiO_2	52.1	58.3	53.3	57.6	65.7	54.1	52.3
TiO_2	1.3	0.6	1.0	0.8	0.7	0.9	0.8
Al_2O_3	16.8	13.6	14.6	13.8	14.0	15.4	16.6
TFeO	10.7	5.3	11.0	9.1	5.3	9.3	8.4
MgO	4.3	9.6	5.5	4.8	2.7	6.0	7.1
MnO	0.2	0.1	0.2	0.1	0.1	0.2	0.1
CaO	8.2	4.5	8.1	6.6	2.7	7.9	9.4
Na_2O	4.0	2.5	3.1	3.0	3.1	3.3	2.6
K_2O	0.7	3.2	1.3	1.7	2.4	1.1	0.6
P_2O_5	0.5	0.1	0.3	0.2	0.1	0.2	0.1
Mg#	0.46	0.79	0.51	0.52	0.52	0.58	0.64
Ba	1165	1434	448	574	652	518	259
Co	29	31	46	35	19	36	38
Cr	73	490	198	221	82	311	215
Ga	22	15	19	18	19	18	13
Hf	7.4	4.6	3.2	3.6	5.2	2.5	1.9
Nb	11	6	9	9	10	7	5
Ni	48	347	85	78	49	147	88
Pb	7.0	12.9	9.7	11.0	16.0	9.7	4.2
Rb	3	51	31	36	93	22	11
Sc	20	20	33	23	14	30	31
Sr	1250	712	387	381	304	381	348
Ta	0.4	0.3	0.6	0.4	0.6	0.4	0.6
Th	1.0	0.5	1.3	2.8	9.2	2.0	1.2
U	0.1	0.2	0.5	0.5	1.3	0.6	0.2
V	151	100	213	147	104	168	196
Y	33	8	15	14	18	23	16
Zr	346	180	125	141	191	130	68
La	58	18	22	23	41	34	8
Ce	117	36	44	46	72	55	20
Pr	15					7.6	2.6
Nd	61	14	23	23	31	29	11
Sm	11	2.6	4.7	4.1	4.9	5.6	2.8
Eu	3.1	1.0	1.4	1.3	1.2	1.3	1.1
Gd	8.2					4.8	3.1
Tb	1.2	0.3	0.7	0.6	0.8	0.9	0.5
Dy	6.1					5.6	3.1
Ho	1.2					1.1	0.7
Er	3.0					2.8	1.9
Tm	0.4						
Yb	2.6	0.8	1.9	1.6	2.0	2.4	1.5
Lu	0.4	0.1	0.3	0.3	0.3	0.4	0.3

Nushan = weighted average lower crust of Nushan; HNB = Modeled composition of Hannuoba Lower crust (Liu et al., 2001); GSKC = average of Archean mafic and intermediate granulite terrains of Sino-Korean Craton (Liu et al., 1999); CSKC = Lower crust of Sino-Korean Craton (Gao et al., 1998a); CYC = Lower crust of Yangtze Craton (Gao et al., 1998a); GWC = average of worldwide Archean mafic and intermediate granulite terrains (Rudnick and Fountain, 1995); R&F = mean composition of the continental lower crust (Rudnick and Fountain, 1995).

(Fig. 2a, 4a; Table 2), Nb and Ta (Fig. 4 h), and higher TiO_2 (Fig. 2b) and FeO contents (Table 2) and Eu positive anomaly (Fig. 3a). This possibly suggests that it represents a cumulate from a relatively evolved liquid and not a solidified melt. These chemical differences possibly indicate a different protolith in agreement with the younger age. However, the isotopic composition of NS202, indistinguishable from that of the other xenoliths (Fig. 7a, b) and characterized by extremely low ε_{Nd} values at 140 Ma (Table 5), is different from the Hannuoba granulites and the Mosozoic volcanic rocks in Eastern China (Fig. 7b). The formation of NS202 would necessarily require assimilation of large amounts of very old lower crust by the crystallizing basalt at 140 Ma (Fig. 7b), which is in consistent with the relatively low Mg# and high TFeO in all Nushan granulite xenoliths (Table 2).

6.2. Physical Properties of the Lower Crust beneath Nushan

6.2.1. P-T estimates and geothermal gradient

The two-pyroxene geothermometers of Wells (1977) and Wood and Banno (1973) are used to estimate the equilibrium temperatures of the Nushan granulites. They yield similar results (804–899 °C, mostly at 850±20 °C; Table 7). These estimates are slightly lower than those of the Hannuoba granulite xenoliths (850–950 °C; Chen et al., 2001).

McCarthy and Patiňo Douce (1998) calibrated an empirical geobarometer (hereafter referred as to MPD barometer) based on the equilibrium between silica, Ca-tschermak's and anorthite. Figure 10 compares pressure estimates on garnet-bearing granulites from worldwide occurrences (Yamamoto, 1993; Ma

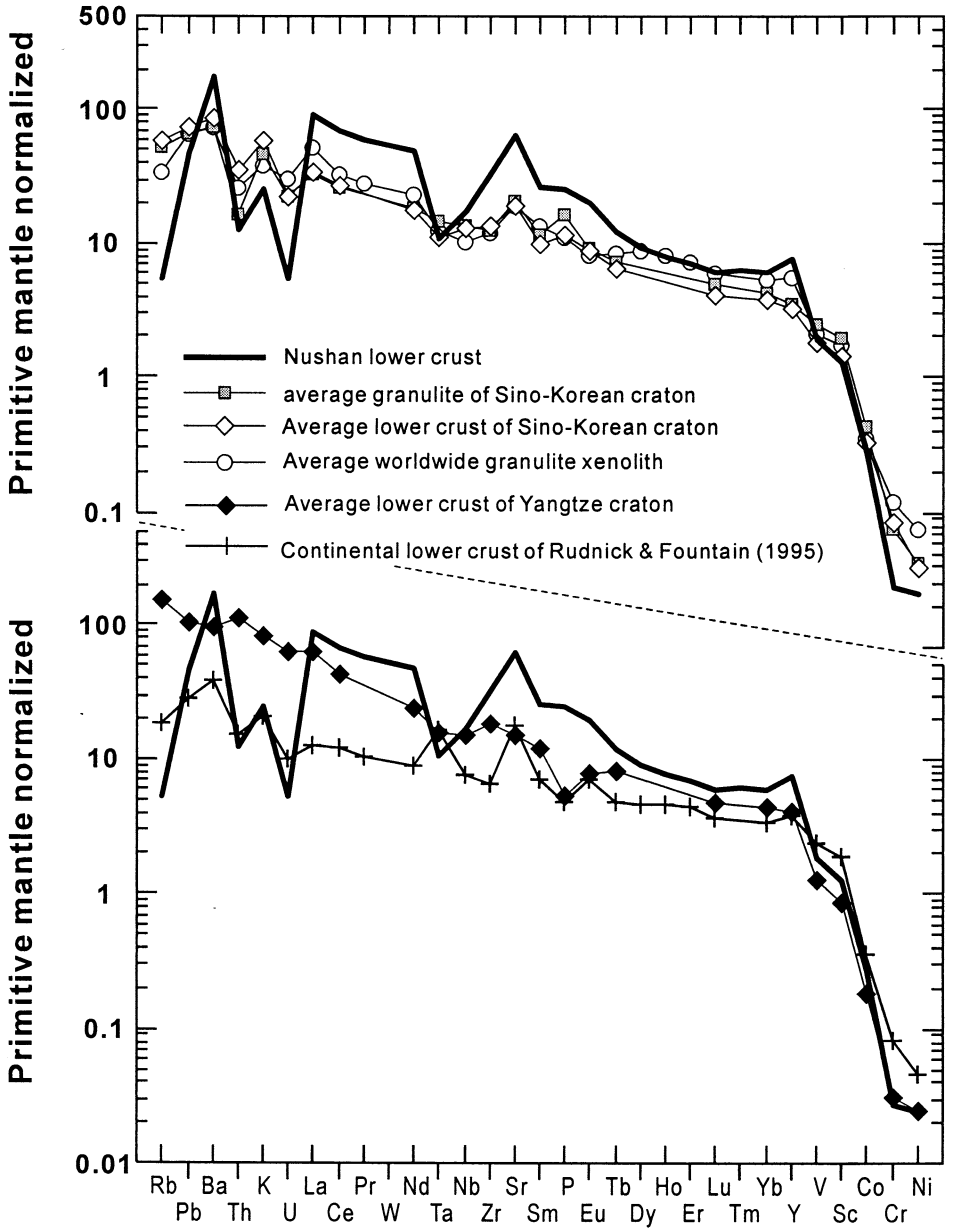

Fig. 13. Average compositions of the Nushan lower crust. All concentrations are normalized to the primitive mantle (McDonough and Sun, 1995).

and Wang, 1994; Stosch et al., 1995; McCarthy and Patiño Douce, 1998) using the MPD barometer (P_{MPD}) and the barometers of Moecher et al. (1988) and Newton and Perkins (1982) (P_{Moe} and $P_{N\&P}$, respectively). The latter two methods are relatively well established and suitable for the assemblages of garnet - plagioclase - orthopyroxene (clinopyroxene) - quartz. P_{MPD} are in good agreement with $P_{N\&P}$ and P_{Moe} when the pressure is greater than 6 kbar. This testifies the feasibility of the MPD barometer to estimate pressure of the granulites that contain no garnets.

The application of this barometer to the Nushan granulite xenoliths yields a wide range of pressure estimates (4.5–9.5 kbar, Table 7). However, most of the Nushan granulites are equilibrated at 6.2–9.5 kbar, corresponding to 20–31 km in depth. The estimates lower than 6 kbar for NS214 and NS217 are considered meaningless, because precedent evaluation suggests that the MPD barometer underestimates pressure when P $<$ 6 kbar (Fig. 10). The equilibrium pressures for the Nushan granulite xenoliths are lower than the typical pressure range (10–15 kbar) for the basalt-borne granulite xenoliths, but are comparable to that typical (6–8 kbar) of the Archean granulite terrains. This is consistent with the similarity in mineral chemistry between the Nushan granulites and the Archean granulite terrains in the SKC.

Xu et al. (1998) have established the Cenozoic geotherm at Nushan based on the garnet-bearing mantle xenoliths. Since the

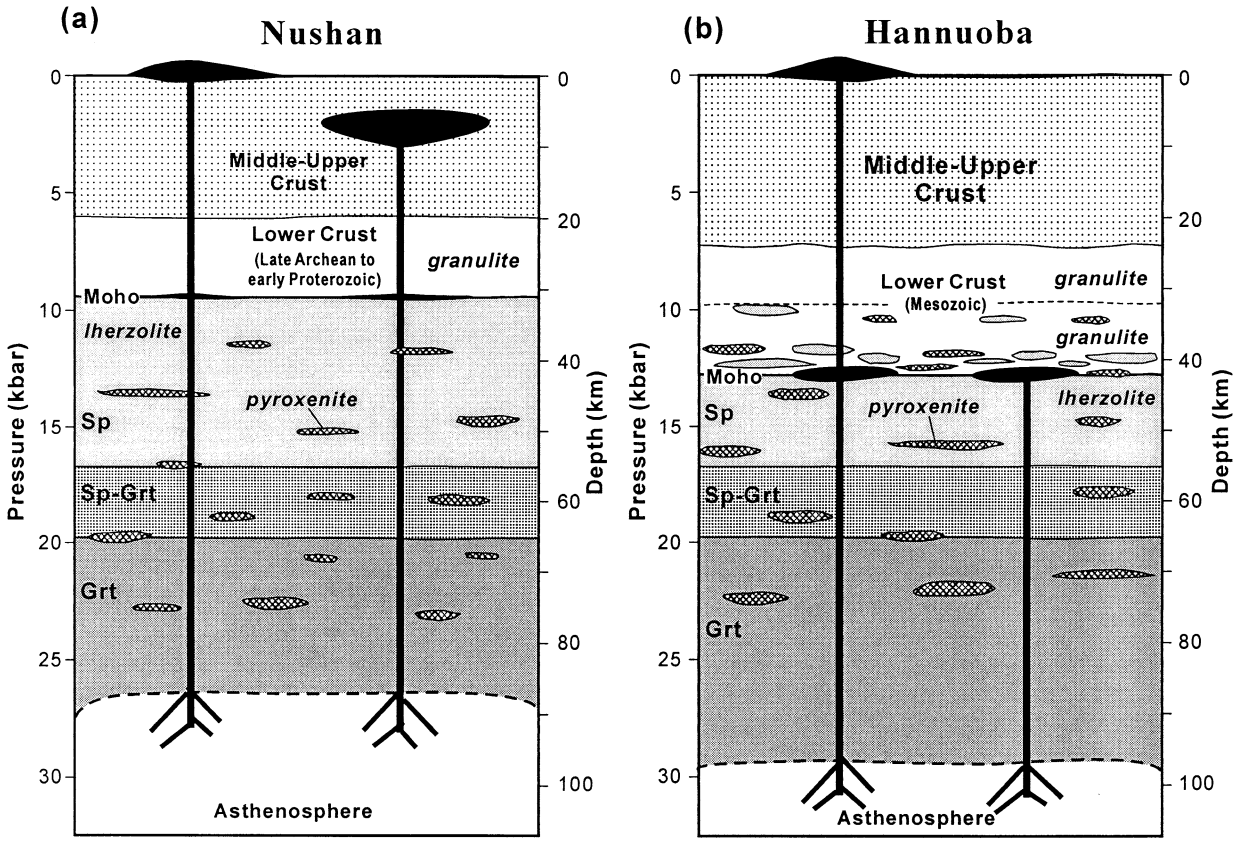

Fig. 14. Lithologic profile of the lower crust and upper mantle at Nushan (a) and Hannuoba (b) (after Chen et al., 2001; Liu et al., 2001).

Nushan garnet-peridotite and pyroxenites are equilibrated at P $>$ 16 kbar and T $>$ 1000 °C, the thermal gradient in the uppermost mantle at Nushan remains poorly constrained. For instance, Xu et al. (1998) extrapolated the thermal gradient of the deep mantle to the shallow level based on a spinel pyroxenite-spinel lherzolite composite xenolith Nu9505. However, the pressure of this composite is poorly constrained. Accordingly, the geotherm around the crust-mantle transition necessitates a verification using other independent data. Such a test is now possible as the equilibrium P-T conditions of the samples from the lower crust are available. As shown in Figure 11, the lower crustal geotherm at Nushan based on the equilibrium T-P of granulite xenoliths is similar to the extrapolated part of Xu et al.'s mantle geotherm. This geotherm corresponds to a high thermal gradient ($\sim$ 80 mW/m^2; Xu et al., 1998).

6.2.2. Depth to the Moho

The "seismic Moho" is defined as the base of the crust, across which the compressional wave velocity increases rapidly to $\sim$8 km/s, whereas the crust-mantle boundary (CMB) is the transition between felsic-mafic crustal rocks and a dominantly ultramafic upper mantle (Griffin and O'Reilly, 1987). They are not always consistent, particularly in continental regions of high heat flow where the seismic Moho may lie deeper than the CMB (Griffin and O'Reilly, 1987). The depth to CMB can be estimated by comparing the temperature estimates of the spinel lherzolites and xenolith-based geotherm (O'Reilly and Griffin, 1985). The equilibrium temperatures for the Nushan granulite xenoliths are all below 900°C, whereas mantle-derived xenoliths are mostly equilibrated at temperatures higher than 900°C (Xu et al., 1998). 900°C is therefore considered as the temperature at the base of the lower crust. By reference of the geotherm in Figure 11, this suggests that the depth to the CMB at Nushan is *ca.* 30 km, consistent with the depth to Moho as revealed by seismic refraction data (Fig. 12; Chen, 1988).

6.2.3. Seismic velocity and structure

The seismic refraction profile (HQ-13) (Fig. 1) suggests a three-layer structure consisting of upper, middle and lower crust at Nushan, and the lower crust ranges in depth from 20–31 km (Fig. 12; Chen, 1988). Such a three-layer structure is markedly different from the four-layer structure widely documented in different tectonic unites in the SKC (Gao et al., 1998a, 1988b), in which a fourth high-velocity layer about 5 km thick occurs in the lowermost crust (Holbrook et al., 1992; Christensen and Mooney, 1995; Rudnick and Fountain, 1995). The viability of the seismic model on the crustal structure can be tested through studying the direct samples from the lower crust. Calculated velocities of granulite xenoliths based on primary mineral compositions and single crystal elastic prop-

erties can effectively eliminate the influence of alteration that significantly reduces the seismic velocities of granulite xenoliths (Rudnick and Jackson, 1995; Gao et al., 2000; Liu et al., 2001), and thus should reflect those of the lower crust. Table 7 presents calculated elastic wave velocities (V_p) of the Nushan granulite xenoliths. The calculated V_2, corrected at the P-T conditions of present-day Nushan lower crust, range from 6.53 to 6.86 km/s (Table 7), which agrees with the observed V_p of the lower crust at Nushan (Fig. 12.

According to Gao et al. (1998b), the upper lower crust in the SKC has velocities of 6.7–6.8 km/s and the lowermost crust has 7.0–7.2 km/s at 600MPa and room temperature. For the purpose of comparison (e.g., Rundnick and Fountain, 1995), the calculated V_p of Nushan granulite xenoliths is also corrected at 600 MPa and room temperature (V_3, Table 7). V_3 ranges from 6.70–7.02 km/s with an average of 6.9 km/s. Only a few mafic samples (e.g., NS202) have $V_p > 7.0$ km/s, which may be the constituents of the lowermost layer in the Nushan crustal section. U-Pb dating shows that the emplacement of mafic magmas took place during the Mesozoic. However, this emplacement may be very weak given the scarcity of the samples with $V_p > 7.0$ km/s.

6.3. Composition of the Lower Crust beneath Nushan and its Tectonic Implication

The composition of the lower crust can be constrained by the studies of chemical composition and depths of the lower crustal xenoliths. Thermobarometric calculation suggests that the Nushan granulites are samples from a depth interval of 20–31 km, which virtually covers all the depth range of the lower crust as defined by seismic data. Moreover, the consistency between calculated velocities of granulites xenoliths and regional seismic refraction data implies that the granulite xenoliths represent the main constituents of the lower crust at Nushan.

The bulk lower crustal composition is calculated by weighting the average compositions of the relevant granulite xenoliths according to the layer thickness they represent. The model composition of the Nushan lower crust is basic with SiO_2 = 52.1 wt.%, distinctively different from the composition of the lower crust of the Yangtze Craton (CYC, Table 8). Although the estimated SiO_2 and Al_2O_3 contents of the Nushan lower crust are similar to those of the continental lower crust defined by Rudnick and Fountain (1995), TFeO, MgO, CaO and Na_2O are significantly different (Table 8). Specifically, the estimated composition at Nushan contains relatively high TFeO (10.7 wt.%) and low MgO (4.3 wt.%) contents. These compositional characteristics are indeed very similar to the averages of Archean granulite terrains in the SKC and of worldwide Archean granulite terrains (Table 8), but are different from the model composition of the lower crust at Hannuoba (HNB, Table 8).

Figure 13 compares the modeled trace element compositions of the Nushan lower crust with those of the lower crust beneath the SKC and the Yangtze Craton (Gao et al., 1998a), Archean granulite terrain of the SKC (Liu et al., 1999) and of continental lower crust based on world-wide granulites (Rudnick and Fountain, 1995). The lower crust beneath Nushan is characterized by strong depletion of Nb, Ta, U and Th with appreciable positive Sr and P anomalies (Fig. 13). These characteristics are essentially similar to those of the lower crust beneath the SKC and of the average composition of the Archean granulites from the SKC, although the Nushan estimates have higher contents of LREE, Ba, Sr, Zr and Hf. In contrast, they are significantly different from the lower crust beneath the Yangtze craton, which is characterized by higher Th and U contents and strong P depletion (Fig. 13). Such a comparison leads to the conclusion that the lower crust beneath Nushan is more likely related to the SKC, rather than being linked to the Yangtze craton. On the other hand, the age of the Nushan intermediate granulites is broadly consistent with the crustal formation events in the SKC. The data presented in this study yield implications for the location of the suture zone between the North and South China Blocks.

While the northern margin of the Qinlin-Dabie Shan orogenic belt is widely considered as the suture zone between the North and South China Blocks to the west of TLFZ (Zhang et al., 1989; Okay and Sengör, 1992), considerable debate prevails on the location of suture to the east of TLFZ (Okay and Sengör, 1992; Li, 1994; Chung, 1999; Zhang, 2000; Chung and Li, 2000). The Su-Lu ultrahigh pressure metamorphic belt is commonly considered as the boundary between the North China and South China Blocks (Okay and Sengör, 1992). However, Li (1994) proposed that the suture zone is located about 300 km south of the Su-Lu ultrahigh pressure terrane. In his crustal-detachment model, Li (1994) suggested that the upper crust of the South China block in the Subei-Yellow Sea region was detached from the lower crust and thrust over the North China for >400 km, whereas the lower lithosphere was subducted under the North China block along a subsurface suture running east from Nanjing (Fig. 1). As Nushan is located at southwestern Subei basin and to east of the TLFZ (Fig. 1), the first model implies an affinity of the lower crust at Nushan to the Yangtze Craton, whereas the second model predicts an affinity to the SKC. The compositional resemblance of the lower crust at Nushan to that beneath the SKC thus supports the crustal-detachment model of Li (1994). Similar conclusions have been reached based on studies of the lower crustal xenoliths from southeast China (Yu et al., 2003) and geochemical and isotope characteristics of Cenozoic basalts around the TLFZ (Chung, 1999).

6.4. Spatial Heterogeneity of the Lower Crust beneath the SKC

A wealth of petrologic and geochemical data is now available on granulite xenoliths from Hannuoba, another important xenolith locality in the northern SKC. A comparison between the granulite xenoliths from Hannuoba and Nushan is therefore necessary to examine the spatial variation in composition of the lower crust beneath the SKC. Figure 14 schematically summarizes the lithological profiles at the two localities, from which several major differences are noted.

(a) The lower crust at Hannuoba (24–42 km) is significantly thicker than that beneath Nushan (20–31 km). Thermobarometric data suggest a shallower derivation of the Nushan granulites (6–9.5 kbar) than the Hannuoba granulites (>10 kbar).
(b) A high velocity layer of 3–5 km thick occurs in the lowermost crust at Hannuoba (Liu et al., 2001). It consists of

granulites with variable proportion of pyroxenites and peridotites (Chen et al., 2001). In contrast, this high velocity layer is not observed in the Nushan case.

(c) The average lower crust at Nushan is more basic (SiO_2 = 52.1%) than that at Hannuoba (SiO_2 = 58.3%, Table 8).

What is the reason for the compositional and structural difference of the lower crust beneath Nushan and Hannuoba? Is the relatively basic character of the Nushan lower crust simply the result of a biased sampling towards mafic composition by the host basalts? Felsic granulites are not found at Nushan. The felsic rocks described by Yu et al. (2003) are indeed gneiss that may be derived from the middle or upper crust. The consistency between the observed and calculated velocities strongly suggests that the Nushan granulites represent the predominant components of the lower crust at this locality, and felsic components, if present, are minor, because a small amount of felsic rocks would considerably lower the velocities. Moreover, the compositional difference between the Nushan and Hannuoba xenoliths is corroborated by the different seismic velocities at the two localities (Ma et al., 1991). Specifically, the velocities of the lower crust to the east of the DTGL including Nushan area are *ca.* 0.2 km/s higher than those to the west of the DTGL (i.e., Hannuoba area), suggesting a more basic lower crust to the east of the DTGL. Therefore, the contrasting composition of the granulites from Nushan and Hannuoba mostly likely reflects the spatial heterogeneity of the lower crust beneath the SKC, rather than an artifact of biased sampling. It is possible that the lower crusts in the eastern and western sides of the DTGL are fundamentally different, as geochronological studies suggest that they were formed at different time. While most of the Nushan xenoliths are late Archean to early Proterozoic in age, the Hannuoba mafic to intermediate granulites represent underplated materials of basalts during the late Mesozoic (Fan and Liu, 1996; Liu et al., 2001). This Mesozoic underplating could be coeval with the initiation of the widespread thermotectonic reactivation of the SKC (Menzies et al., 1993; Griffin et al., 1998; Xu, 2001). However, the Mesozoic underplating under the Nushan region may have not been a major process according to the data presented in this work.

The different extent of Mesozoic underplating at Nushan and Hannuoba may be related to the heterogeneous lithospheric extension in these regions. Nushan lies close to the southern part of the *trans*-lithospheric Tan-Lu fault zone (Fig. 1), which represents one of the weakest lithospheric segments in the SKC. The lithosphere along this fault zone is significantly thinner than that beneath rift basins (Ma, 1989). In this mechanically weakened zone, mantle-derived magmas could traverse efficiently the crust-mantle boundary and intrude into middle-upper crust or erupt to the surface. This is consistent with voluminous Mesozoic (165–100 Ma) volcanic rocks (Wang et al., 1996) and dioritic and gabbroic intrusives (Xu et al., 1993; Guo et al., 2001) in Shandong Province (Fig. 1) that is cross-cut by the Tanlu fault. In contrast, Hannuoba is located west to the DTGL, where the lithospheric extension was less intense and the lithosphere is generally thicker than that beneath the eastern part of the SKC (Ma, 1989). Under this circumstance, mantle-derived magmas were trapped at the CMB due to density contrast. Repeated underplating of basalts would result in a vertical crustal growth, giving rise to the formation of a thick crust-mantle transition zone at Hannuoba (Fig. 14). The effect of lithospheric extension on underplating processes in continental setting is also supported by geophysical data. The Xiangshui to Mandal geo-transect (XMGT, Fig. 1) shows ubiquitous existence of the high velocity lowermost crust under the SKC except for the regions adjacent to the TLFZ (Ma et al., 1991).

6.5. Implications for the Xenolith versus Terrain Issue

It has been recognized for a long time that granulite xenoliths are more mafic than granulite terrains (Rudnick, 1992). However, the Nushan granulite xenoliths are surprisingly similar in composition to exposed Archean granulite terrains, but are somewhat different from basalt-borne xenoliths from worldwide occurrences. This particularity sheds lights on the origin of the compositional distinction between granulite xenoliths and terrains. As discussed in previous sections, the peculiar composition of the lower crust beneath Nushan is somehow related to the absence of major magmatic underplating in this region. This is a rare case because Cenozoic basaltic fields are commonly associated with magmatic underplating at the crust-mantle boundary, which resulted in the formation of ubiquitous high velocity layer below the preexisting “old” crust (Gao et al., 1998b). As most xenoliths were collected from Cenozoic basalts in extended regions, it is likely that a large portion of xenoliths may come from the newly accreted mafic layer and/or overlaying hybrided zones. This may explain the compositional difference between granulite xenoliths and terrains.

7. CONCLUSIONS

The granulite xenoliths from Nushan are compositionally similar to the Archean granulite terrain in the SKC, but are distinctively different from the Hannuoba mafic granulite xenoliths, which are mainly metamorphosed products of underplated materials during late Mesozoic. The protolith of the Nushan granulites was subjected to crystal fractionation and interaction with old continental crustal rocks. Zircon U-Pb dating further suggests that the magmatic underplating took place at *ca.* 2.5 Ga and granulite-facies metamorphsim peaked at 1.9 Ga. This old lower crust possibly underwent minor basaltic underplating during the Mesozoic (117–140 Ma). Most of the Nushan granulite xenoliths probably represent samples from the late Archean to early Proterozoic crystalline basement beneath the SKC.

Thermal gradient in the lower crust constructed based on the equilibrium P-T conditions of the Nushan granulites is consistent with that extrapolated from the mantle geotherm (Xu et al., 1998). The depth to the CMB inferred from this revised geotherm agrees with the depth to the seismic Moho (~ 30 km). This, together with the consistency between calculated velocities of granulite xenoliths and observed V_p structure, strongly suggests that there is no high-velocity lowermost crust at Nushan, and the granulite xenoliths represent the dominant components in the lower crust at this locality. The absence of the high velocity lowermost layer at Nushan contrasts with the thick crust-mantle transition zone at Hannuoba, and can be ascribed to intense lithospheric extension along major translithospheric faults that facilitated mantle-derived magmas traverse the CMB to reach shallow levels or the surface. The modeled composition of the Nushan lower crust is more basic

than that at Hannuoba. Such a compositional difference is correlated with the difference of average V_p of the lower crust in the two areas. All these imply two fundamentally different lower crustal structures in the western and eastern sides of the DTGL.

The comparison between the Nushan and Hannuoba granulite xenoliths yields implication for the long-last issue regarding the compositional difference between granulite xenoliths and terrains. Mafic feature of the granulite xenoliths relative to granulite terrains is probably due to widespread magmatic underplating in Cenozoic volcanic fields from which the xenoliths are collected.

Acknowledgments— We gratefully acknowledge the constructive comments by S. Gao and two anonymous reviewers which helped improve the manuscript. We also like to thank Y. Liu, X.R. Liang, P. Jian and B. Song for technical assistance with ICP-MS, Sr-Nd isotope analyses and SHRIMP dating. Discussion with Dr. X.H. Li was very helpful. This study is supported by the National Nature Science Foundation of China (49925308).

Associate editor: M. Menzies

REFERENCES

Bhattacharyya C. (1971) An evaluation of the chemical distinctions between igneous and metamorphic orthopyroxenes. *Am. Mineral.* **56,** 499–506.

Bohlen S. R. and Mezger K. (1989) Origin of granulite terranes and the formation of the lowermost continental crust. *Science* **244,** 326–329.

Chapman D. and Furlong K. (1992) Thermal state of the continental crust. In *Continental Lower Crust* (eds. D. M. Fountain, R. Arculus, and R. W. Kay), Elsevier Sci., New York. pp. 179–200.

Chen D. G. and Peng Z. C. (1988) K-Ar ages and Sr, Pb isotopic characteristics of Cenozoic volcanic rocks in Jiangsu and Anhui provinces. *Acta Petrolog. Sin.* **4,** 3–12 (in Chinese with English abstract).

Chen H. S. (1988) The essentials of geological-geophysical integrated interpretation of the Line HQ-13 in the lower Yangtze Basin on the Yangtze Metaplatform. In *Petroleum Exploration in Southern China* (ed. Q.X. Ou). Geological Publishing House, Beijing. pp. 239–250. (in Chinese with English abstract).

Chen S. H., O'Reilly S. Y., Zhou X. H., Griffin W. L., Zhang G. H., Sun M., Feng J. L., and Zhang M. (2001) Thermal and petrological structure of the lithosphere beneath Hannuoba, Sino-Korean Craton, China: evidence from xenolith. *Lithos* **56,** 267–301.

Christensen N. I. and Mooney W. D. (1995) Seismic velocity structure and composition of the continental crust: A global view. *J. Geophys. Res.* **100,** 7961–7988.

Chung S.-L. (1999) Trace element and isotope characteristics of Cenozoic basalts around the Tanlu fault with implications for the eastern plate boundary between North and South China. *J. Geol.* **107,** 301–312.

Chung S.-L. and Li Z.-X. (2000) Trace element and isotope characteristics of Cenozoic basalts around the Tanlu fault with implications for the eastern plate boundary between North and South China: A reply. *J. Geol.* **108,** 743–748.

Compston W., Williams I. S., and Meyer C. (1984) U-Pb geochronology of zircons from lunar breccia 73217 using a sensitive high mass-resolution ion microprobe. *J. Geophys. Res.* **89,** B525–534.

DePaolo D. J. (1981) Trace element and isotopic effects of combined wallrock assimilation and fractional crystallization. *Earth Planet. Sci. Lett.* **53,** 189–202.

Downes H. (1993) The nature of the lower continental crust of Europe: Petrological and geochemical evidence from xenoliths. *Phys. Earth Planet. Inter.* **79,** 195–218.

Fan Q. C. and Liu R. X. (1996) High temperature granulite xenoliths in Hannuoba basalts. *Chinese Sci. Bull.* **41,** 235–238 (in Chinese).

Fan Q. C., Liu R. X., Li H. M., Sui J. L., and Lin Z. R. (1998) Zircon chronology and REE geochemistry of granulite xenoliths at Hannuoba. *Chinese Sci. Bull.* **43,** 1510–1515.

Fan Q. C., Sui J. L., Liu R. X., and Zhou X. M. (2001) Eclogite facies garnet-pyroxenolite xenoliths in Hannuoba area: new evidence of magma underplating. *Acta Petrol. Sin.* **17,** 1–6 (in Chinese with English abstract).

Gao S., Kern H., Liu Y. S., Jin S. Y., Popp T., Feng J. L., Jin Z. M., Sun M., and Zhao Z. B. (2000) Measured and calculated seismic velocities and densities for granulites from xenoliths occurrences and the adjacent exposed lower crustal sections: A comparative study from the North China craton. *J. Geophys. Res.* **105,** 18965–18976.

Gao S., Luo T. C., Zhang B. R., Zhang H. F., Han Y. W., Zhao Z. D., and Hu Y. K. (1998a) Chemical composition of the continental crust as revealed by studies in East China. *Geochim. Cosmochim. Acta* **62,** 1959–1975.

Gao S., Zhang B. R., Jin Z. M., Kern H., Luo T. C., and Zhao Z. D. (1998b) How mafic is the lower continental crust? *Earth Planet. Sci. Lett.* **161,** 101–117.

Gebrande H. (1982) Elasticwave velocities and constants of elasticity of rocks-forming minerls. In *Physical Properties of Rocks, Vol. 1b* (ed. G. Angenheister), pp. 1–96. Springer-Verlag, New York.

Griffin W. L. and O'Reilly S. Y. (1987) Is the continental Moho the crust-mantle boundary? *Geology* **15,** 241–244.

Griffin W. L., Zhang A. D., O'Reilly S. Y. and Ryan C. G. (1998) Phanerozoic evolution of the lithosphere beneath the Sino-Korean craton. In Mantle Dynamics and Plate Interactions in East Asia (eds. M. F. J. Flower, S. L. Chung, C. H. Lo and T. Y. Lee). AGU Geodynamics Series 27, pp. 107–126.

Guo F., Fan W. M., Wang Y.-J., and Lin G. (2001) Late. Mesozoic mafic intrusive complexes in North China Block: constraints on the nature of subcontinental lithospheric mantle. *Phys. Chem. Earth* **26A,** 759–772.

Guo J. H., Zhai M. G., Li Y. G., and Yan Y. H. (1998) Contrasting metamorphic P-T paths of Archean high-pressure granulites from the North China craton: metamorphism and tectonic significance. *Acta Petrol. Sin.* **14,** 430–448. (in Chinese with English abstract).

Guo J. H., Zhai M. G., Li Y. G., Yan Y. H., and Zhang W. H. (1994) Isotopic ages and their tectonic significance of metamorphic rocks from middle part of the early Precambrian granulite belt, North China craton. In *Geological Evolution of the Granulite Terrain in North Part of the North China Craton* (eds. X. L. Qian and R. M. Wang), pp. 130–144. Seismological Press, Beijing (in Chinese with English abstract).

Holbrook W. S., Mooney W. D., and Christensen N. I. (1992) The seismic velocity structure of the deep continental crust. In *Continental Lower Crust* (eds. D. M. Fountain, R. Arculus, and R. W. Kay), pp. 1–43. Elsevier Sci, New York.

Huang X. L. and Xu Y. G. (2002) Geochemical characteristics of the Nushan granulite xenoliths, Anhui province: implications for composition of lower crust and tectonic affinity. *Geochim.* **32,** 443–454. (in Chinese with English abstract).

Huang X. L., Xu Y. G., Chu X. L., Zhang H. X., and Liu C. Q. (2001) Geochemical comparative studies of some granulite terranes and granulite xenoliths from North China craton. *Acta Petrol. Mineral.* **20,** 318–328. (in Chinese with English abstract).

Jahn B. M. (1990) Origin of granulites: Geochemical constraints from archean granulite facies rocks of the Sino ~ Korean craton, China. In *Granulites and Crustal Evolution* (eds. D. Vielzeuf and Ph Vidal), pp. 471–492. Kluwer Academic Publishers, Netherlands.

Jahn B. M. and Zhang Z. Q. (1984) Archean granulite gneisses from eastern Hebei Province, China: rare earth geochemistry and tectonic implications. *Contrib. Mineral. Petrol.* **85,** 224–243.

Jahn B. M., Auvray B., Cornichet J., Bai Y. L., Shen Q. H., and Liu D. Y. (1987) 3.5 Ga old amphibolites from eastern Hebei province, China: field occurrence, petrography, Sm ~ Nd isochron age and REE geochemistry. *Precamb. Res.* **34,** 311–346.

Jahn B. M., Auvray B., Shen Q. H., Liu D. Y., Zhang Z. Q., Dong Y. J., Ye X. J., Zhang Q. Z., Cornichet J., and Mace J. (1988) Archean crustal evolution in China: the Taishan complex, and evidence for Juvenile crustal addition from long-term depleted mantle. *Precamb. Res.* **38,** 381–403.

Kempton P. D. and Harmon R. S. (1992) Oxygen isotope evidence for large-scale hybridization of the lower crust during magmatic underplating. *Geochim. Cosmochim. Acta* **56,** 971–986.

Kempton P. D., Downes H., and Embey-Isztin A. (1997) Mafic granulite xenoliths in Neogene alkali basalts from the Western Pannonian Basin: insights into the lower crust of a collapsed orogen. *J. Petrol.* **38,** 941–970.

Li Z. X. (1994) Collision between the North and South China blocks: a crustal-detachment model for suturing in the region east of the Tanlu fault. *Geology* **22,** 739–742.

Liu C. Q., Masuda A., and Xie G. H. (1994) Major- and trace-element compositions of Cenozoic basalts in eastern China: Petrologenesis and mantle source. *Chem. Geol.* **114,** 19–42.

Liu D. Y., Nutman A. P., Compston W., Wu J. S., and Shen Q. H. (1992) Remnants of 3800 crust in the Chinese Part of the Sino-Korean craton. *Geology* **20,** 339–342.

Liu F. L. (1997) The metamorphic reaction and water activity of basic granulite in the Datong-Huaian region. *Acta Petrol. Sin.* **13,** 27–43. (in Chinese with English abstract).

Liu Y., Liu H. C., and Li X. H. (1996) Simultaneous and precise determination of 40 trace elements in rock samples by ICP-MS. *Geochim.* **25,** 552–558. (in Chinese with English abstract).

Liu Y. S., Gao S., and Luo T. C. (1998) HFSE in the mafic volcanic rocks in north China craton: implications for the Ar-Pt boundary and Cenozoic basalts mantle source. *Earth Sci. J. China Univ. Geosci.* **23,** 468–474. (in Chinese with English abstract).

Liu Y. S., Gao S., and Luo T. C. (1999) Geochemistry of granulites in North China craton: Implications for the composition of Archean lower crust. *Geol.Geochemistry* **27,** 40–46. (in Chinese with English abstract).

Liu Y. S., Gao S., Jin S. Y., Hu S. H., Zhao Z. B., and Feng J. L. (2001) Geochemistry of lower crustal xenoliths from Neogene Hannuoba basalt, North China Craton: implication for petrogenesis and lower crustal composition. *Geochim. Cosmochim. Acta* **65,** 2589–2604.

Lu S. N. (1998) Geochronology and Sm-Nd isotopic geochemistry of Precambrian crystalline basement in eastern Shandong Province. *Earth Sci. Front. (China Univ. Geosci., Beijing)* **5,** 275–283. (in Chinese with English abstract).

Ma J. and Wang R. M. (1994) Reviews in garnet-clinopyroxene geothermometers and geobarometers with their application to granulite: the comparison of Miyun (Zunhua) and Xuanhua granulite forming condition. In *Geological Evolution of the Granulite Terrain in North Part of the North China Craton* (eds. X. L. Qian and R. M. Wang), pp. 71–88. Seismological Press, Beijing. (in Chinese with English abstract).

Ma X. (1989) Atlas of active faults in China. Seismological press, Beijing. pp. 1–120.

Ma X. Y., Liu C. Q., and Liu G. D. (1991) Xiangshui (Jiangsu Province) to Mandal (Inner Mongolian) geoscience transect. *Acta Geol. Sin.* **65,** 199–215. (in Chinese with English abstract).

McCarthy T. C. and Patiño Douce A. E.. (1998) Empirical calibration of the silica - Ca - tschermak's - anorthite (SCAn) geobarometer. *J. Metamorph. Geol.* **16,** 675–686.

McDonough W. F. and Sun S.-s. (1995) The composition of the Earth. *Chem. Geol.* **120,** 223–253.

Menzies M. A. and Xu Y. G. (1998) Geodynamics of the North China craton. In *Mantle Dynamics and Plate Interactions in East Asia* (eds. M. F. J. Flower, S. L. Chung, C. H. Lo, T. Y. Lee). AGU Geodynamics Series 27, pp. 155–165.

Menzies M. A., Fan W. and Zhang M. (1993) Paleozoic and cenozoic lithoprobes and the loss of >120km of archaean lithosphere, Sino-Korean craton, China. In *Magmatic Processes and Plate Tectonics* (eds. H. M. Prichard, T. Alabaster, N. B. W. Harris and C. R. Neary). *Geol. Soc. Spel. Pub.* **76,** 71–81.

Moecher D. P., Essene E. J., and Anovitz L. M. (1988) Calculation and application of clinopyroxene-garnet-plagioclase-quartz geobarometers. *Contrib Mineral Petrol.* **100,** 92–106.

Moorbath S. and Taylor P. N. (1986) Geochronology and related isotope geochemistry of high-grade metamorphic rocks from the lower continental crust. In *The Nature of the Lower Continental Crust* (eds. J. B. Dawson, D. A. Carswell, J. Hall and K. H. Wedepohl). *Geol. Soc. Spec. Publ.* **24,** 211–220.

Newton R. C. and Perkins D. (1982) Thermodynamic calibration of geobarometers based on the assemblages garnet-plagioclase-orthopyroxene (clinopyroxene)-quartz. *Am. Mineral.* **67,** 203–222.

O'Reilly S. Y. and Griffin W. L. (1985) A xenolith-derived geotherm for southeastern Australia and its geological implications. *Tectonophys.* **111,** 41–63.

Okay A. I. and Sengör A. M. C. (1992) Evidence for continental thrust-related exhumation of the ultra-high- pressure rocks in China. *Geology* **20,** 411–414.

Rietmeijer F. J. M. (1983) Chemical Distinction between igneous and metamorphic orthopyroxenes especially those coexisting with Ca-rich clinopyroxenes: a re-evaluation. *Mineral. Mag.* **47,** 143–151.

Rudnick R. L. (1992) Xenoliths-samples of the lower continental crust. In *Continental Lower Crust* (eds. D. M. Fountain, R. Arculus, and R. W. Kay), pp. 269–316. Elsevier Sci., New York.

Rudnick R. L. and Fountain D. M. (1995) Nature and composition of the continental crust: A lower crustal perspective. *Rev. Geophys.* **33,** 267–309.

Rudnick R. L. and Jackson I. (1995) Measured and calculated elastic wave speeds in partially equilibrated mafic granulite xenoliths: Implications for the properties of an underplated lower continental crust. *J. Geophys. Res.* **100,** 10211–10218.

Shaw D. M. (1972) The origin of the Apsley gneiss, Ontario. *Can. J. Earth Sci.* **9,** 18–35.

Shen Q. H., Zhang Z. Q., Xu H. F., and Ji C. L. (1994) Early Precambrian Granulites of China. Geological Publishing House, Beijing. pp. 62–73.

Stosch H.-G., Ionov D. A., Puchtel I. S., Galer S. J. G., and Sharpouri A. (1995) Lower crustal xenoliths from Mongolia and their bearing on the nature of the deep crust beneath central Asia. *Lithos.* **36,** 227–242.

Sun S.-s. and McDonough W. F. (1989) Chemical and isotopic systematics of oceanic basalts: implications for mantle composition and processes. In *Magmatism in the Ocean Basins* (eds. A. D. Saunders and M. J. Norry), pp. 313–345. Geological Society, London.

Wang D. Z., Ren Q. J., Qiu J. S., Chen K. R., Xu Z. W., and Zen J. H. (1996) Characteristics of volcanic rocks in the shoshonite province, eastern China, and their metallogenesis. *Acta Geolog. Sin* **70,** 23–34. (in Chinese with English abstract).

Wells P. R. A. (1977) Pyroxene thermometry in simple and complex systems. *Contrib. Mineral. Petrol.* **62,** 129–139.

Williams I. S. (1992) Some observations on the use of zircon U-Pb geochronology in the study of granitic rocks. *Trans. R. Soc. Edinburgh - Earth Sci.* **83,** 447–458.

Williams I. S., Buick I. S., and Cartwright I. (1996) An extended episode of earlhy Mesoproterozoic metamorphic fluid flow in the Reylolds Range, central Australia. *J. Metamorph. Geol.* **14,** 29–47.

Wood B. J. and Banno S. (1973) Garnet-orthopyroxene and orthopyroxene-clinopyroxene relationships in simple and complex systems. *Contrib. Mineral. Petrol.* **42,** 109–124.

Xu W. L., Chi X. G., Yuan C., Huang Y. M., and Wang W. (1993) Mesozoic dioritic rocks and deep-seated inclusions in central north China platform. Geological Publishing House, Beijing. pp. 1–164. (in Chinese).

Xu X. S., O'Reilly S. Y., Griffin W. L., Zhou X. M. and Huang X. L. (1998) The nature of the cenozoic lithosphere beneath Nushan, East Central China. In *Mantle Dynamics and Plate Interactions in East Asia* (eds. M. F. J. Flower, S. L. Chung, C. H. Lo and T. Y. Lee). AGU Geodynamics Series 27, pp. 167–196.

Xu Y. G. (2001) Thermo-tectonic destruction of the Archaean lithospheric keel beneath the Sino-Korean Craton in China: evidence, timing and mechanism. *Phys. Chem. Earth* **26A,** 747–757.

Xu Y. G. (2002) Evidence for crustal components in the mantle and constraints on crustal recycling mechanisms: pyroxenite xenoliths from Hannuoba, North China. *Chem. Geol.* **182,** 301–322.

Xu Y. G. and Bodinier J.-L. Contrasting enrichments in high and low temperature xenoliths from Nushan, Eastern China: Results of a single metasomatic event during lithospheric accretion? *J. Petrol.* (in press).

Yamamoto H. (1993) Contrasting metamorphic P-T-time paths of the Kohistan granulites and tectonics of the western Himalayas. *J. Geol. Soc. London* **150,** 843–856.

Yu J. H., Xu X. S., O'Reilly S. Y., Griffin W. L., and Zhang M. (2003) Granulite xenoliths from Cenozoic Basalts in SE China proveide geochemical fingerprints to distinguish lower crust terranes from the North and South China tectonic blocks. *Lithos.* **67,** 77–102.

Zhai M. G., Guo J. H., Yan Y. H., Li Y. G., Li J. H., and Zhang W. H. (1996) An Oblique cross section of Archaean continental crust in Shanxi-Hebei-Nei Mongol juncture area, North China Craton. *Acta Petrol. Sin.* **12,** 222–238. (in Chinese with English abstract).

Zhang G., Yu Z., Sun Y., Cheng S., Li T., Xue F., and Zhang C. (1989) The major suture zone of the Qinling orogenic belt. *J. SE Asian Earth Sci.* **3,** 63–76.

Zhang K. J. (2000) Trace element and isotope characteristics of Cenozoic. basalts around the Tanlu fault with implications for the eastern plate boundary between North and South China: An extended discussion. *J. Geol.* **108,** 739–742.

Zhao G. C., Wilde S. A., and Cawood P. A. (1999) Thermal evolution of two textual types of maficgranulites in the North China craton: Evidence for both mantle plume and collisional tectonics. *Geol. Mag.* **136,** 223–240.

Zhou X. H., Sun M., Zhang G. H., and Chen S. H. (2002) Continental crust and lithospheric mantle interaction beneath North China: isotopic evidence from granulite xenoliths in Hannuoba, Sino-Korean cration. *Lithos.* **62,** 111–124.

Zhou X. M., Yu J. H., and Xu X. S. (1992) Discovery and significance of granulite xenoliths in the Nushan basalt, East China. *Chi. Sci. Bull.* **37,** 1730–1734.